THE JOURNAL OF PHYSICAL CHEMISTRY C

pubs.acs.org/JPCC

Feature Article

Shapes, Plasmonic Properties, and Reactivity of Magnesium Nanoparticles

Emilie Ringe*

Cite This: J. Phys. Chem. C 2020, 124, 15665−15679

Read Online

ACCESS | Metrics & More | Article Recommendations

ABSTRACT: Localized surface plasmon resonances have attracted much attention due to their ability to enhance light−matter interactions and manipulate light at the subwavelength level. Recently, alternatives to the rare and expensive noble metals Ag and Au have been sought for more sustainable and large-scale plasmonic utilization. Mg supports plasmon resonances, is one of the most abundant elements in earth's crust, and is fully biocompatible, making it an attractive framework for plasmonics. This feature article first reports the hexagonal, folded, and kite-like shapes expected theoretically from a modified Wulff construction for single crystal and twinned Mg structures and describes their excellent match with experimental results. Then, the optical response of Mg nanoparticles is overviewed, highlighting Mg's ability to sustain localized surface plasmon resonances across the ultraviolet, visible, and near-infrared electromagnetic ranges. The various resonant modes of hexagons, leading to the highly localized electric field characteristic of plasmonic behavior, are presented numerically and experimentally. The evolution of these modes and the associated field from hexagons to the lower symmetry folded structures is then probed, again by matching simulations, optical, and electron spectroscopy data. Lastly, results demonstrating the opportunities and challenges related to the high chemical reactivity of Mg are discussed, including surface oxide formation and galvanic replacement as a synthetic tool for bimetallics. This Feature Article concludes with a summary of the next steps, open questions, and future directions in the field of Mg nanoplasmonics.

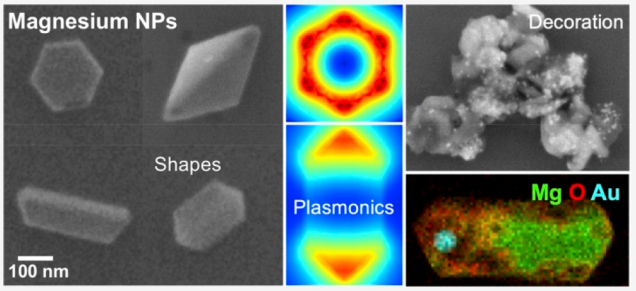

INTRODUCTION

Over the past decades, nanotechnology has revealed a multitude of fascinating new phenomena. An emerging theme is that, at the nanometer scale, shape and size control the properties of materials, including optical, magnetic, chemical, and electronic, to name a few.

A particularly active field of research benefiting from this opportunity is that of nanoparticles (NPs) of free-electron metals such as Al, Cu, Au, and Ag. Indeed, they attract much interest owing to their ability to support localized surface plasmon resonances (LSPRs), a resonant oscillation of conduction electrons driven by the oscillating electric field of light. LSPRs give rise to enhanced, wavelength-dependent light absorption, light scattering, and local confinement of the electric field in the nanoscale region near the NP's surface. Plasmon resonances can therefore, in principle, be useful whenever strong electric fields or enhanced light−matter interactions are sought. Applications, developed over the past decades and constantly evolving, range from hyperthermia-based cancer treatment[1−5] to surface-enhanced spectroscopies,[6−11] chemical and biological sensors,[12−17] photocatalysts,[18−23] and optical waveguides.[24,25]

To optimize a system based on plasmonic NPs, one must fine-tune their optical response. For instance, the absorption/scattering ratio should be maximized for photothermal applications,[26−28] while the strength and decay length of the local electric field can be focused for surface enhanced spectroscopies[6,16,29,30] and the peak width, minimized for efficient refractive index sensing.[13−16] Manipulating these properties can be done *via* size, shape, and composition control, generating much interest in the understanding of crystal growth and shapes as well as the development of synthetic and fabrication approaches. These are now mature fields for the most common plasmonic NPs, of Ag and Au, for which an extensive array of shapes can be achieved and rationalized.

However, Ag and Au are rare and expensive, and Ag suffers from sustained oxidation and tarnishing, significantly affecting its optical properties in a matter of hours to days in air.[31,32] Efforts to find viable alternative plasmonic materials that are earth-abundant have been met with limited success. Indeed, very few elements and compounds have the dielectric properties

Received: April 30, 2020
Revised: June 10, 2020
Published: June 12, 2020

https://dx.doi.org/10.1021/acs.jpcc.0c03871
J. Phys. Chem. C 2020, 124, 15665−15679

required to sustain strong resonances, namely a small positive imaginary and large negative real dielectric constant, ideally across the ultraviolet (UV), visible and infrared (IR).[33−37] A possible candidate, Cu, is cheaper than Au but more lossy[35] across its visible to IR operating range, leading to weaker, broader resonances. Most importantly, Cu suffers from rapid (~hours or less) and complete oxidation to a non-plasmonic oxide when in contact with water or air.[38,39] Al is a newer but increasingly well-known plasmonic metal, with resonances in the UV and visible up to ~700 nm owing to a strong interband transition leading to high losses at lower energies.[34,40,41] Self-limiting surface oxidation stabilizes Al NPs in organic solvents.[42] Other metals have been considered, including Hg, Gd, and In, as well as compounds such as indium-doped tin oxide (ITO) and TiN; these have been discussed and reviewed elsewhere.[33,43−48]

Perhaps one of the newest plasmonic metals is Mg. It has a broad operating range and an unusual, compared to Al, Cu, Ag, and Au at least, hexagonal crystal structure. Recent experimental work has demonstrated that top-down fabricated Mg nanostructures sustain LSPRs. For instance, Mg helices exhibit a chiral photoresponse,[49] disk arrays fabricated by hole-mask colloidal lithography interact strongly with visible light,[50] and aperture films enhance fluorescence radiation rates.[51] In addition to showing plasmon-driven enhanced light-matter interactions, Mg has the remarkable ability to switch from a plasmonic state, when Mg is metallic, to the non-plasmonic MgH_2 phase upon reaction with H_2.[50,52,53] Return to a plasmonic state, fully reversibly, occurs with the introduction of O_2; the process can be enhanced by a thin catalyst layer (such as Pd/Ti[50]). Such switching provides a platform not only for hydrogen storage and sensing[54−56] but also for dynamic nanoplasmonics that can cover the entire visible color range, with potential application in displays.[57,58] Incidentally, Mg-based pixels irreversibly disintegrate in water, putting into question their robustness as a technological product although creating opportunities for stealth, biodegradable messaging.[59]

While they provided the foundations of Mg plasmonics, these fabricated structures are rough and polycrystalline, leading to several drawbacks, including enhanced oxidation,[41] transformation kinetics varying from grain to grain,[52] and lower quality plasmon resonances.[60,61] In parallel, the synthesis of small Mg particles has gained momentum in the hydrogen storage community[54−56] seeking enhanced surface area to volume ratios. Meanwhile, Mg NPs have been demonstrated to enhance light absorption for biocompatible photothermal cancer therapy by Locatelli et al.[5] and colleagues in Martin et al.,[1] albeit the authors do not mention the NP's plasmonic behavior, nor do they characterize them optically. Our recent demonstration of size-dependent LSPRs in both the far-field and the near-field for colloidally synthesized Mg NPs[62,63] brought together some of the field's nascent ideas and started new research efforts with exciting prospects for novel plasmonic shapes and properties.

In this Feature Article, results on the crystalline, optical, and chemical properties of nanostructured Mg will be highlighted. First, the unusual shapes adopted by single crystalline and twinned Mg NPs will be discussed in the rigorous framework of the Wulff construction. Then, the focus will shift on the plasmonic response of various Mg NP shapes, probed with both numerics and experiments for both optical and electron beam excitation. Lastly, the challenges and opportunities related to the high reactivity of Mg will be considered, including decoration *via* galvanic replacement, and oxidative stability. Together, these results constitute the seed of the nascent field of colloidal Mg nanoplasmonics.

RESULTS AND DISCUSSION

Crystallography and Unusual Shapes of Mg. Mg crystallizes as hexagonal close packed (HCP, space group $P6_3/mmc$, a = 320.94 pm, c = 521.08 pm). This is unlike all other mainstream plasmonic metals (Al, Cu, Ag, Au) that adopt the same face-centered cubic (FCC) structure. The shapes of FCC crystals, formed by roughly a quarter of the elements (Figure 1),

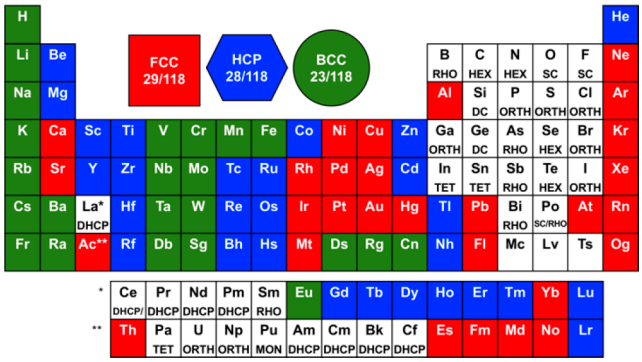

Figure 1. Stable crystal structure of the elements. Together, face-centered cubic (FCC), hexagonal close packed (HCP), and body-centered cubic (BCC) account for ~68% of stable crystal structures. Other structures are rhombohedral (RHO), hexagonal (HEX), simple cubic (SC), orthorhombic (ORTH), diamond cubic (DC), tetragonal (TET), double hexagonal close packed (DHCP), and monoclinic (MON). Data from refs 64 and 65. The structures of Mc, Lv, and Ts are uncertain.

are well-understood and several protocols exist to control shape and twinning. Meanwhile, HCP metals are equally common yet much less is known about their synthesis and shapes in colloidal, metallic (nonoxidized) form.

Both HCP and FCC are close-packed lattices, the former possessing an ABAB packing of close-packed planes, and the latter, ABCABC. This results in anisotropy in the HCP lattice, as the c-direction is unlike the equivalent a and b directions. This anisotropy bestowed by the different packing sequence leads to different low-energy planes in HCP than in FCC, hence differences in exposed surfaces and twin planes. HCP and FCC thus have drastically different crystal shapes.

Before shapes are explored, the nomenclature in hexagonal systems will be reviewed to avoid any confusion. In most crystal systems, planes are described by the Miller indices (hkl); families of planes are referred to as $\{hkl\}$. Directions use the $[UVW]$ notation, families, $\langle UVW\rangle$. As an example, the planes (100), (010), and (001) are equivalent and part of the $\{100\}$ family of planes in the cubic system. This nomenclature can apply to hexagonal systems but yields unrelated set of indices for symmetry-equivalent planes, for instance, the $(1\bar{1}0)$ and (100). To remedy this, the u-axis is constructed as to be 120° from both a and b; then Miller−Bravais indices $(hkil)$ are used, with $i = -(h + k)$.[66] Now the equivalent planes $(1\bar{1}00)$ and $(10\bar{1}0)$ are in the $\{1\bar{1}00\}$ family of planes and have similar indices. The convention for directions utilizing the Weber symbols $\langle UVTW\rangle$ is not as straightforward nor broadly adopted; fortunately, it is not needed here.

In HCP, the plane basal to the unit cell and perpendicular to the c-direction, (0001), is close-packed (Figure 2), and therefore

https://dx.doi.org/10.1021/acs.jpcc.0c03871
J. Phys. Chem. C 2020, 124, 15665−15679

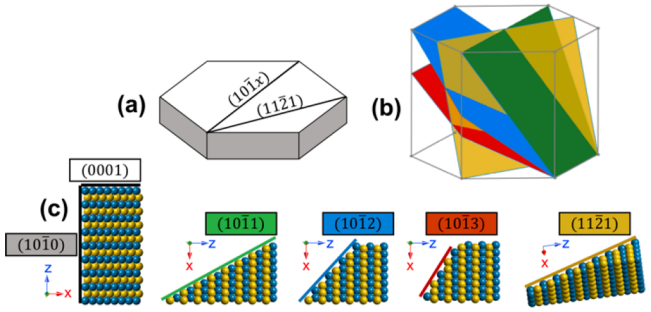

Figure 2. Mg crystallography and twin planes. (a) Aerial view of a hexagonal plate showing the relative orientation of the $(10\bar{1}x)$ and $(11\bar{2}1)$ planes. (b) Position and orientation of the planes within the hexagonal unit cell of Mg, following the color coding of (c). (c) Atomic packing of facets (0001) and $(10\bar{1}0)$, and twin planes, $(10\bar{1}x)$ with x = 1, 2, 3 and $(11\bar{2}1)$. The alternating ABAB close-packed layers of Mg are represented in alternating blue and yellow atoms. (a) and (b) adapted with permission from ref 62. Copyright 2020 American Chemical Society.

has the lowest surface free energy (γ) in the absence of other factors (e.g., in a vacuum). The pair (0001) and $(000\bar{1})$ directions are the only two close-packed planes in the structure; they are not symmetry equivalent to the unit cell's other bounding facets of which $(10\bar{1}0)$ and $(01\bar{1}0)$ are examples. This is unlike the FCC structure where the low-energy planes, {111}, have eight equivalent orientations (four pairs) perpendicular to a body diagonal of the unit cell. In addition, HCP has multiple densely packed planes, as shown in Figure 2. These include $\{10\bar{1}x\}$, where, when x = 0, these are parallel to the c axis and then, as x increases from 1 to 3, the planes tilt downward and become more scarcely packed. Planes of type $(11\bar{2}y)$ are also of low energy, with the most densely packed nonparallel to c among those, $(11\bar{2}1)$, shown in Figure 2. Together, these are the most likely planes to be expressed at the surface of a crystal and serve as twin planes.

The relative surface energy and orientation of planes in a crystal dictates its habit, i.e., its shape, as explained by Wulff over a century ago.[67] Wulff stated that the shortest (i.e., perpendicular) distance between the center of a crystal and a crystal facet is proportional to the surface energy of that facet. In FCC, a low {111} energy followed by a modest {100} energy leads to the thermodynamic cuboctahedron shape sometimes laxly referred to as "the Wulff shape". In HCP, the Wulff construction implies a short distance for the lowest energy {0001} planes and the formation of platelets with hexagonal shapes.

This mathematical approach to predicting shapes from surface energies can be adapted to twinned crystals as introduced by Marks[68] and further developed by Ringe, Van Duyne and Marks[69] to introduce kinetic effects and match shapes experimentally obtained. In short, segments are assembled along the appropriate twin plane, with the shape of each segments obtained from a (truncated) Wulff construction. Recently, Boukouvala and Ringe encoded this in a simple graphical user interface (GUI) we now call Crystal Creator.[70] The package, shown in Figure 3, models the shape of a crystal based on twinning and relative surface energies; a conformal shell of arbitrary thickness can also be added. The shape is exported as a figure or a fully formatted SHAPE file, i.e., the dipole array used as an input for calculating near- and far-field plasmonic behavior using the discrete dipole approximation

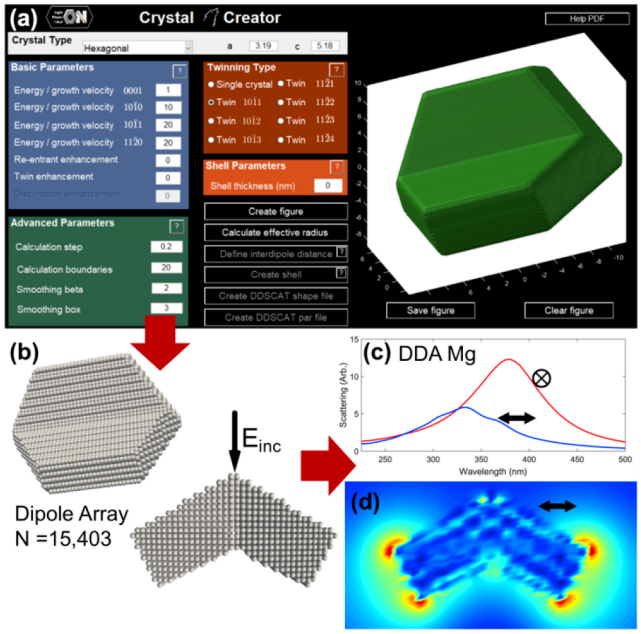

Figure 3. Crystal Creator, a Wulff-based approach to generate cubic and hexagonal crystal shapes including twins and shells. (a) The graphical user interface generates an array of dipoles as shown in (b) for a tent NP. This array can then be exported as a DDSCAT-formatted file to perform numerical simulations of the (c) far-field and (d) near-field plasmonic response.

(DDA) in the numerical package DDSCAT for optical excitation[71−73] or e-DDA[74] for electron beam excitation. In Figure 3, a Mg tent NP with 15 403 dipoles has been generated by the code and used to calculate the optical scattering response in DDSCAT for a beam traveling along the NP's bisector with polarization along the long (longitudinal) and short (transverse) NP axis. The associated local electric field at the tips of the NP with transverse excitation is also shown as an example of the numerical results enabled by combining Crystal Creator and DDSCAT.

The graphical user interface, initially published for cubic structures by Boukouvala and Ringe,[70] and now augmented to include shape modeling for hexagonal systems with various twins, is available, in its most up-to-date form, free of charge on the group's Web site, https://www.on.msm.cam.ac.uk/code.html.

This Wulff construction tool and the numerical simulations it enables are invaluable to predict and understand the shape and optical behavior (see next section) of plasmonic NPs, for both FCC and HCP. In FCC Al, Cu, Ag, and Au, twinning occurs on {111} planes and there can be 2, 5, or 20 segments, leading to bipyramidal, decahedral, and icosahedral shapes, respectively; this array of possible shapes and compositions indeed provides a rich repertoire of plasmonic response for the FCC metals. In the less well-studied HCP Mg, twinning can readily occur along multiple planes, namely, the $(10\bar{1}x)$ with x = 1, 2, and 3 and $(11\bar{2}y)$ with y = 1, 2, 3, and 4.[62,75,76] This complex twinning behavior suggests a plethora of crystal habits for particles with the same number of segments (2) and equivalent relative surface energies (Figure 4).

Many of the unusual shapes predicted by the Wulff construction for twinned HCP NPs have been observed experimentally for Mg, some 40 years ago by Ohno et al. from gas-phase NP deposition[76] and many more colloidally by

https://dx.doi.org/10.1021/acs.jpcc.0c03871
J. Phys. Chem. C 2020, 124, 15665−15679

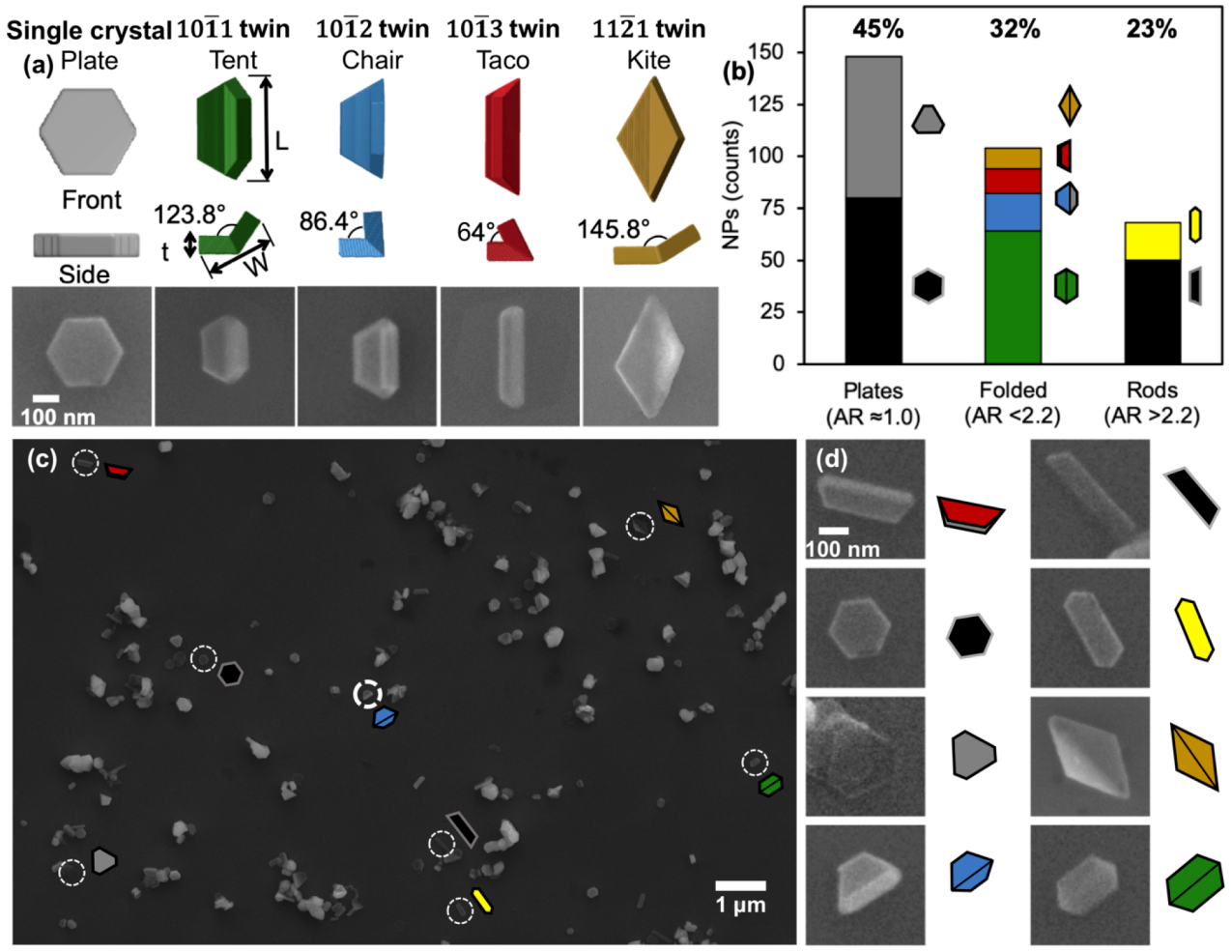

Figure 4. Shapes of single crystalline and singly twinned Mg NPs. (a) Predictions from the Wulff model (top) and scanning electron microscopy (SEM) images, all on the same scale, of reaction products for a single crystal, tent, chair, taco and kite. (b) Shape distribution from 320 NPs. Plates (AR ~ 1) include hexagons and truncated hexagons; folded structures (AR < 2.2) are kites (orange), tacos (red), chairs (blue), and tents (green); rods (AR > 2.2) include filled chairs (black) and truncated plates (yellow). (c) Large-scale SEM image of various NPs and aggregates, with examples of structures identified and reported in (d). Adapted with permission from ref 62. Copyright 2020 American Chemical Society.

Asselin, Boukouvala et al. this year,[62] as shown in Figure 4. Similar to single crystals, the twinned NPs are bound by the low energy {0001} and {10$\bar{1}$0} facets. The NPs containing a (10$\bar{1}x$) twin plane with x = 1, 2, and 3 form ten-facet structures akin to folded hexagons with increasingly small folding angles of 123.8° (tent), 86.4° (chair), and 64.0° (taco), respectively. Of the comparatively higher energy twin planes (11$\bar{2}y$), only y = 1 has been experimentally observed. The resulting shape is a folded structure resembling a kite, this time with only eight facets due to the orientation of the twin plane.

NPs of twinned Mg can rest in one of two orientations on a substrate, which we call Λ and ≥. The Λ configuration is the highest symmetry where the NP sits with the folding bisector perpendicular to the substrate, as in the bottom right NP, a tent, in Figure 4. NPs in the ≥ configuration have one of the {0001} facets in intimate contact with the substrate (tent in Figure 4a). For hexagonal plates these configurations are identical.

These shapes are strikingly different from the {111}-twinned FCC NPs, offering opportunities for novel near-field light localization. Further, these are only one set of shapes, obtained in the same reaction mixture and thus with the same {0001}:{10$\bar{1}$0} relative surface free energy. For each type of twin, various AR and shapes are possible given different surface energies, suggesting a vast new playing field for plasmonic light control, including local field distribution and polarization effects.

While these numerous shapes present a thrilling range of opportunities, they also lead to intrinsic issues of high heterogeneity. Indeed, the small differences in twin energies between the many possible twinning orientations means many types of nuclei are formed within the same reaction mixture. Growth then occurs according to the relative surface energies dictated by the material and the reaction conditions. While in principle each type of seed should lead to only one shape, the final product nevertheless contains a shape mixture because of the twinning mixture. This heterogeneity, from flat plates to long narrow tacos, leads to significant broadening of the optical response of bulk solutions, a challenge for shape-property characterization but a possible advantage when considering absorption of a broadband emitter such as the sun.

LSPR Response in the UV, Visible, and Near-IR: Theoretical Considerations. Free electron metals such as Mg, Al, Cu, Ag, and Au can sustain strong plasmon resonances in some or all of the UV, visible, and near-IR region of the electromagnetic spectrum. The ability to sustain such resonances is encoded in the frequency-dependent complex dielectric function ϵ:

https://dx.doi.org/10.1021/acs.jpcc.0c03871
J. Phys. Chem. C 2020, 124, 15665−15679

$$\epsilon = \epsilon' + i\epsilon'' \quad (1)$$

where ϵ' and ϵ'' are the real and imaginary parts, respectively. In the bulk solid, the vanishing of the real part corresponds to its volume plasmon resonance, at frequency ω_p, and the accompanying transition from optical transparency (above ω_p) to opacity (below ω_p). In contrast, the imaginary part describes optical absorption inside the medium, which damps and diminishes the resonance. In metals, such damping is largely attributed to interband transitions, i.e., the promotion of a single particle from the valence to conduction bands.

In metallic nanoparticles, lower frequency plasmon resonances, LSPRs, exist and are associated with excitations at the interface of the metal and the surrounding medium. These occur when the real part of the dielectric function is sufficiently negative relative to the surrounding medium, as exemplified by the (Fröhlich) condition for the dipole resonance of a sphere: $\epsilon' = -2\epsilon_{medium}$; conditions vary with the order of the resonance and the shape of the NP.[77,78] Thus, a good plasmonic material has a dielectric function with a small imaginary part and a large span of negative real parts, enabling many and strong resonances.

There are no interband transitions in Mg across the UV, visible and NIR owing to its electronic structure (s-metal),[37] such that it has relatively low losses (small ϵ'') across this range. In contrast, Au and Cu have interband transition onsets in the blue region of the visible, and Al has a relatively sharp interband contribution centered near 800 nm. Further, omitting interband effects, the magnitude of ϵ' increases when moving away from the plasma frequency ω_p; a ω_p far above the region of interest is thus desirable and is achieved in Mg (10.6 eV) and Al (15 eV[79]) because of a large number of electrons in the conduction band on a per atom basis (2 and 3, respectively).

The dielectric functions of Cu, Ag, Au, Al, and Mg, shown in Figure 5a,b, provide a basis for comparison of the quality and operating range of these common plasmonic metals. It is immediately obvious that Ag is far less lossy (small ϵ'') than most metals from 300 nm onward; it does indeed sustain narrow resonances, but oxidation and scarcity limit its practical applicability. The loss profiles of Ag and its potential alternatives can be summarized as follows:

- In the UV, Mg, Al, and Ag have low losses, the latter only past ~300 nm. Cu and Au suffer from significant losses due to interband transitions.
- In the violet to blue region (~380−520 nm), Cu and Au are still unsuitable, while the losses for the other metals remain low.
- In the green to red region (~520−740), losses in Cu, Ag, and Au are low; Mg and Al's increase with wavelength, with Mg being consistently less lossy than Al.
- In the near-IR, the noble metals slowly become increasingly lossy, while Al displays a dramatic peak near 800 nm (in both real and imaginary parts) owing to interband transitions. Mg displays higher losses than Al past 940 nm for the first time past 200 nm.

Further to the inspection of the losses, the performance of plasmonic materials can be assessed on the basis of the LSPR quality factor, Q_{LSPR}, which includes both the real and imaginary parts of the dielectric function and is defined[15,33,45] as

$$Q_{LSPR} = -\frac{\epsilon'}{\epsilon''} \quad (2)$$

This figure of merit is reported across the UV, visible, and near-IR for Mg, Al, Cu, Ag, and Au in Figure 5c in a semilog plot for clarity. Ag's resonances are of overwhelmingly higher quality across most of the range plotted. Cu and Au do not sustain LSPRs in the blue and higher energy, again due to interband transitions, and perform well in the red and IR. Lastly, Mg outperforms Al in the entire visible range and even at its fringe.

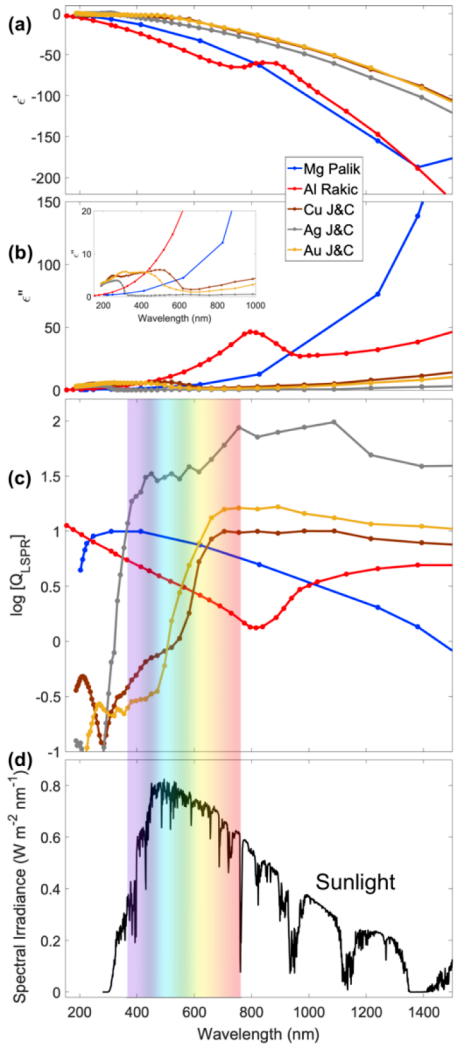

Figure 5. Indicators of plasmonic behavior for Mg and the more common plasmonic metals Al, Cu, Ag, and Au. (a) Real and (b) imaginary part of the dielectric function from published values in Palik,[34] Rakić,[36] and Johnson and Christy (J&C).[35] (c) Log of the LSPR quality factor Q_{LSPR} as defined in eq 2. (d) Solar spectral irradiance,[80] overlaid with the approximate color of the visible range of the electromagnetic spectrum.

An exciting application of plasmonics is light-driven catalysis, especially if it utilizes naturally abundant sunlight. For comparison purposes, a standard spectrum of solar spectral irradiance, hemispherical on 37° tilted surface of the Earth (matching the conditions in the contiguous USA[80]), is plotted in Figure 5d and the approximate location of colors extended to Figure 5c. Materials with quality factors that are high and/or track the solar spectrum are good candidates for sustainable catalysis based on plasmonic effects. Mg performs remarkably well at the peak of the solar spectrum, second only to Ag, and significantly better than the other earth-abundant metal, Al.

Of course, results of the analysis of a metal's dielectric function are only an estimate as they do not include effects such as radiative damping, defect scattering, substrate contributions

https://dx.doi.org/10.1021/acs.jpcc.0c03871
J. Phys. Chem. C 2020, 124, 15665−15679

(if present), and inhomogeneous broadening in a bulk sample.[60,81] Nevertheless, they help provide a comparison platform and a sunny outlook for Mg that encourages systematic experimental verification. Further encouraging numerical predictions for Mg, also yet to be matched with experimental evidence, have been reported for properties such as heat power delivered,[37] near-field enhancement,[37] absorption efficiency,[45] and dielectric functions of alloys such as MgAg.[82]

Plasmonic Behavior of Crystalline Mg Nanoparticles. Inspired by the exciting predicted plasmonic properties of Mg and their systematic experimental verification in fabricated structures, our recent results focus on the understanding of plasmon modes in well-defined, faceted Mg nanocrystals. Plasmonic NPs made from in-principle scalable colloidal syntheses offer significant advantages over fabricated structures, including potential for exceptional shape/size control and homogeneity,[83−85] reduced acoustic vibration damping,[60] smoother surfaces leading to narrower LSPRs,[61,86,87] and avoidance of damping from oxide inclusions within the structures,[41] to name a few. Such features have fueled research into colloidal approaches, which are now mature for Ag and Au, increasingly well-known for Al and Cu, and still in early stages for Mg.

Through these studies, we employ both (far-field) optical scattering and (near-field) electron energy loss spectroscopy, matched with numerical results utilizing the discrete dipole approximation. The optical scattering of single particles immobilized on a transparent substrate is obtained with a dark-field setup in an optical microscope and correlated with electron microscopy.[88−91] The dipole commonly dominates the scattering spectrum, with some contributions from retardation-enabled higher order modes at wavelengths no smaller than ∼375 nm owing to the operating range of the optics and camera used. LSPRs can also be excited locally by an electron in scanning transmission electron microscope electron energy loss spectroscopy (STEM-EELS), where the spatial distribution and energy of plasmon modes is mapped with nanometer resolution, enabling the identification of the resonance energy and symmetry (dipole, quadrupole, etc.).[92−94] STEM-EELS is a powerful tool for the analysis of plasmonics in general, and Mg plasmonics in particular because it reports a broad energy range (sub-1 eV to 1000s of eV), capturing the large array of LSPR energies possible in Mg as well as the bulk plasmon mode at ω_p = 10.6 eV, signature of metallic Mg.

Shape Effects. A simple and common shape produced by Mg is a thin hexagonal plate. This is predicted by the Wulff construction for a single HCP crystal (Figure 4a) and described by early synthesis papers.[54,95,96] We synthesized these structures with tip-to-tip lengths ranging from ∼150 to 300 nm and studied them experimentally with optical (dark-field scattering) and electron (monochromated STEM-EELS) excitation in Biggins, Yazdi, and Ringe.[63] These results were supported by extensive numerical studies obtained using the DDA for optical (DDSCAT[71−73]) and electron (e-DDA modified from ref 74) excitation showing an array of modes spanning the UV, visible, and near-IR.

The first seven LSP modes in hexagonal Mg NPs obtained numerically are shown in Figure 6 and map directly to the first seven solutions to the Helmholtz equation in a hexagon. Given they both are determined by these solutions, the LSP modes match those published for hexagonal waveguides.[97] The two low energy modes are the edge-to-edge and tip-to-tip dipoles, which are degenerate in energy. The next modes are two also-

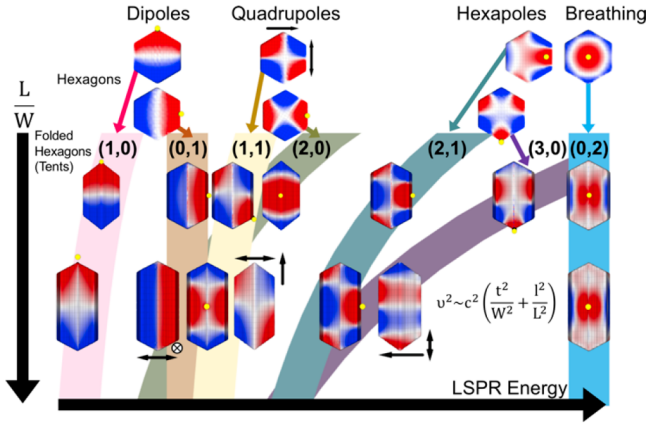

Figure 6. Mode evolution from hexagons to elongated, $(10\bar{1}1)$-twinned folded hexagons (tents). Energy increases from left to right, and AR, L/W, increases from top to bottom. Red and blue coloring represents the magnitude and sign of the electric field perpendicular to the surface of the NP, calculated either with an electron beam excitation (a yellow dot indicates the position of the incident beam) or with plane wave excitation (single arrows point in the propagation direction, double arrows represent the polarization). The (l, t) notation applies to the tent NPs, and the thick bars are plots of eq 3 for each mode, overlaid by the NPs at approximately L/W (AR) = 1.7 and 2.2. Both eq 3 and experimental data indicate a change in the order of energy of the (1, 1) and (2, 0) LSPRs as AR increases. Adapted with permission from refs 63 and 62. Copyrights 2018 and 2020 American Chemical Society.

degenerate quadrupoles. Following are the nondegenerate tip and edge hexapoles (sometimes referred to as sextupoles), where the edge hexapole is of higher energy, and finally a radial breathing mode is expected at higher energy.[98]

Experimental STEM-EELS data, obtained for nine hexagonal NPs of different sizes, match extremely well the modes predicted by e-DDA (Figure 7a,b). First, at low energy, dipolar modes are excited and produce a donut-shaped EEL probability. The spatial distribution of the excitation probability for the next modes are not as simple, since in this size range nondegenerate modes are very close in energy. The experimental data show a single Gaussian-like peak that we call mode 2 at higher energy than the dipole, with strong excitation probability at the NP's tips. Numerical results show that this is in fact the excitation of the quadrupoles and the tip hexapole; however, they cannot be resolved using EELS owing to their extensive spectral and spatial overlap, not even with the advanced spectral deconvolution techniques previously successful at extracting plasmon modes.[19,99−101] The LSPR next higher in energy displays experimental loss probability high at the edges and center of the NP; numerical results attribute this to exciting both the edge hexapole and breathing mode. Further modes are present with ever-increasing overlap as the spacing between modes narrows with rising energy.

The twinning of Mg along $(10\bar{1}x)$ and $(11\bar{2}y)$ produce folded and kite structures that display plasmon modes inherited from those of single crystal hexagonal plates. However, the modes become richer because much of the degeneracy observed in hexagonal plates is lifted by the increase in projected aspect ratio (AR) caused by the folding and elongation along the twin plane. In tents, for instance, the shortest possible projected AR, from folding a hexagon, is 1.31. Experimental ARs range from 1.2 to 2.2: ARs lower than 1.31 are due to corner rounding, and the larger ones are explained by preferential deposition and growth along the twin plane.[69,70] The ARs of the other folded and kite

https://dx.doi.org/10.1021/acs.jpcc.0c03871
J. Phys. Chem. C 2020, 124, 15665−15679

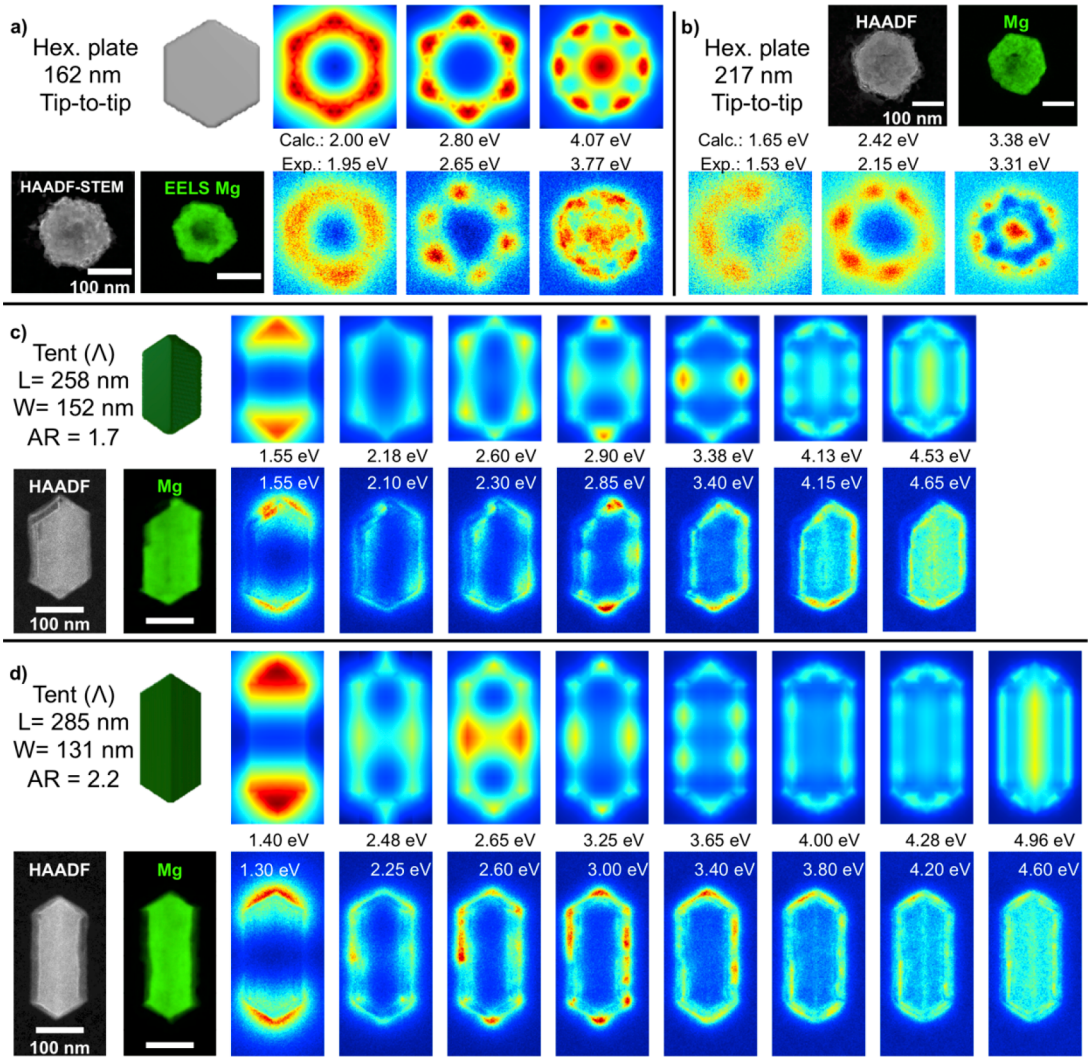

Figure 7. Calculated and experimental near-field plasmonic properties of (a, b) Mg hexagonal plates and tent NPs of AR (c) 1.7 and (d) 2.2. Schematics of the Crystal Creator-generated shapes are shown in gray (hexagonal plates) or dark green (tents in the Λ configuration with respect to the substrate). For each NP, the following are reported: information about size, a HAADF-STEM image, bulk Mg EELS plasmon map (10.6 eV, green), e-DDA-calculated EEL excitation maps (except for (b)), and experimental EELS maps. The experimental maps are integrated across 0.05 eV centered at the labeled energy. The EELS intensity scale is the same across each NPs to allow direct comparison. Adapted with permission from refs 63 and 62. Copyrights 2018 and 2020 American Chemical Society.

shapes are similarly in the 1.2−2.2 range while rod-like structures such as filled chairs and truncated hexagons reach ARs of up to 8.

In the case of folded and rod-like shapes, the simple multipole nomenclature of modes is unsatisfactory; a more appropriate notation is (l, t), where l represents the number of nodes along the length of the particle (longitudinal) and t is the number of nodes along its width (transverse). Starting with a hexagon, the l direction can be set from tip-to-tip and the t as an edge-to-edge perpendicular to l. The dipoles are thus (1, 0) and (0, 1), the quadrupoles are both (1, 1), the hexapoles are (1, 2, tip) and (2, 1, edge), and the breathing mode is (2, 2). In elongated NPs, the previously degenerate modes split and change into resonances that follow the relative energy of standing wave frequencies (υ) for the modes in an $L \times W$ rectangle with nodes (l, t), where c is the speed of light:

$$\upsilon^2 \sim c^2\left(\frac{l^2}{L^2} + \frac{t^2}{W^2}\right) \quad (3)$$

This implies that modes with nodes along the long axis will be more stable than modes with the same number of nodes along the short axis; as the AR increases, long axis nodes decrease in energy. The splitting and evolution of modes from a hexagon to a tent with AR = 2.2 is shown in Figure 6. The dipoles split into longitudinal dipole (1, 0) and transverse dipole (0,1), with the (1, 0) of lowest energy as expected since the NP is, by definition, longer in the longitudinal than the transverse direction. One of the hexagon's quadrupoles becomes the tent's (1, 1) with one node along the twin plane and the other its perpendicular. The other quadrupole transforms into the (2, 0) mode by joining the oscillation phase in the middle of the NP, thereby annihilating one transverse node and creating an extra longitudinal node. Similarly, the (2, 1) edge hexapole retains its pattern, while the (1, 2) corner hexapole turns into the (3, 0) longitudinal mode. The radial breathing mode of the hexagon becomes the (0, 2) transverse higher order mode. A number of additional modes with energy above that of (3, 0) are also present, including the (3, 1) and mixed l modes, as discussed in more detail in ref 62. Lastly, as the AR increases beyond 2.2, longitudinal modes $(l, 0)$

https://dx.doi.org/10.1021/acs.jpcc.0c03871
J. Phys. Chem. C 2020, 124, 15665−15679

become dominant and numerous, as observed by STEM-EELS for Mg nanorods with AR of up to 8.0.[62]

The spatial distribution of the many modes in Mg tents is shown for two NPs in Figure 7c,d. The experimental and numerical field patterns and energies convincingly match for both small and large AR NPs, in part because of our understanding of the NP shape and its orientation with respect to the substrate and our ability, with Crystal Creator, to add an oxide shell and thus match experimental conditions.

The energy of the longitudinal dipole (1, 0) resonance in hexagonal, folded, and kite structures is determined by the length of the particle, consistent with the concept of plasmon length.[102] Indeed, NPs with the same tip-to-tip distance have comparable longitudinal dipole energies, as shown in Figure 8

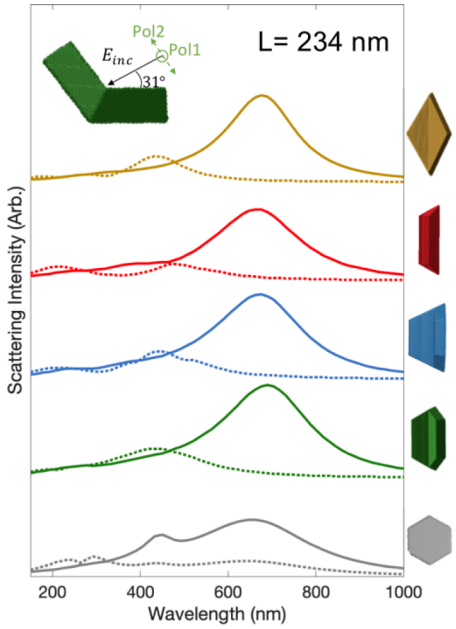

Figure 8. Numerical results on the optical scattering by Mg NPs of different shapes with the same length, L = 234 nm, coated with a ∼4.5 nm MgO layer in a vacuum. From top to bottom, a kite (yellow), taco (red), chair (blue), tent (green), and hexagonal plate (gray). Incident field direction (E_{inc}) and polarizations are shown in the inset. Solid lines represent polarization along the long axis (Pol1); dashed lines, polarization along the short axis (Pol2). Adapted with permission from ref 62. Copyright 2020 American Chemical Society.

for 234 nm long NPs. Similarly to tents of different AR, the relative intensity and energy of higher order modes vary significantly from shape to shape. This is evident in the spectral signature from 200 to 600 nm in Figure 8; further studies are underway to fully characterize these differences, in particular in the near field. The varied shapes afforded by twinning in Mg NPs thus provide opportunities to sculpt the energy and localization of strongly enhanced electromagnetic "hot spots" across the many high order modes present.

Size Effects. LSPRs spanning the UV, visible, and near-IR can be obtained with Mg NPs and are modulated by NP size, a hallmark of plasmonic behavior. The hexagonal plates' mode energies shown in Figure 9 were extracted by Gaussian fitting of the STEM-EELS data set, while the sizes, defined as tip-to-tip, were measured from the HAADF-STEM images acquired during the same experiment. STEM-EELS results from nine hexagonal plates measuring from 162 to 273 nm show plasmons

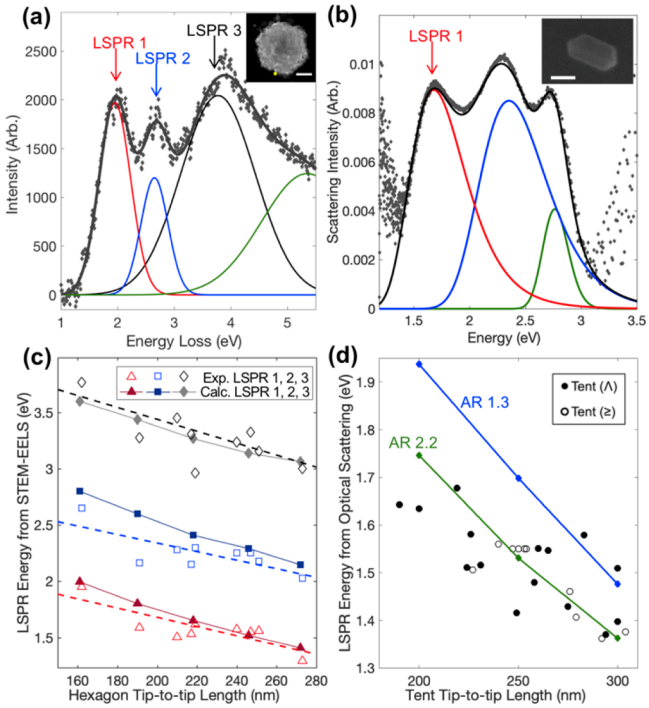

Figure 9. Size effects on the LSPRs of Mg NPs. Experimental (a) Mg hexagonal plate EEL and (b) Mg tent optical dark field scattering spectrum. The insets in both (a) and (b) show the associated HAADF-STEM image and SEM image, respectively; both have scale bars of 100 nm. (c) Experimental and e-DDA-calculated EEL mode energy for modes 1, 2, and 3 as labeled in (a). (d) Experimental and DDA-calculated optical scattering mode energy for the dipole labeled LSPR1 in (b). Adapted with permission from refs 63 and 62. Copyrights 2018 and 2020 American Chemical Society.

from 1.29 eV (960 nm) for mode 1 in the largest NP to 3.77 eV (330 nm) and beyond for mode 3 in the smallest NP. The three lowest energy modes, keeping in mind that modes 2 and 3 are each superpositions of two LSPRs, display a statistically significant size dependence. These trends are well matched by numerical results performed for oxide-coated NPs on a substrate.

STEM-EELS results on tents and rods also show size dependence (e.g., Figure 7c,d), albeit these are more difficult to correlate because of the additional effects of AR, requiring much more data. Size effects were revealed using a higher throughput approach: correlated spectral scanning hyperspectral dark-field optical microscopy[81,88] and scanning electron microscopy (SEM). Data for 25 tents of various AR sitting either with their fold bisector perpendicular to the substrate (Λ configuration), or one of their {0001} facets parallel to the substrate (≥), is shown in Figure 9d, with an example for a single correlated measurement in Figure 9b. The energy of the longitudinal dipole, labeled LSPR1 in Figure 9b, varies as a function of length for tents of different AR in a statistically significant manner (Figure 9d). The other modes are generally weak and difficult to fit, as is obvious from the numerical predictions in Figure 8, and experimental optical results has not yet yielded statistically significant trends. The match with numerical (DDA) results obtained for oxide-coated tent NPs of various ARs on a substrate is moderate (Figure 9d). The discrepancies can be attributed to variations in both metal and oxide thickness as well as imperfect shapes due to etching. Note that the substrate orientation has little effect on the longitudinal

https://dx.doi.org/10.1021/acs.jpcc.0c03871
J. Phys. Chem. C 2020, 124, 15665−15679

dipole energy, as shown by the distribution of filled and empty circles; we observed and calculated[62] that it does however have a marked effect on higher order modes and field localization.

Chemical Properties: Opportunities and Challenges. *Galvanic Replacement.* Unlike established plasmonic materials (Cu, Ag, Au), Mg is far from noble,[103] as shown in Table 1.

Table 1. Standard Reduction Potential (E^o) against the Standard Hydrogen Electrode (SHE) at 25 °C and 1 atm[103]

reaction	E^o (V) vs SHE
$Li^+ + e^- \rightleftharpoons Li$	−3.0401
$Mg^{2+} + 2e^- \rightleftharpoons Mg$	−2.372
$Al^{3+} + 3e^- \rightleftharpoons Al$	−1.662
$Fe^{3+} + 3e^- \rightleftharpoons Fe$	−0.037
$Cu^{2+} + 2e^- \rightleftharpoons Cu$	0.3419
$Ag^+ + e^- \rightleftharpoons Ag$	0.7996
$Pd^{2+} + 2e^- \rightleftharpoons Pd$	0.951
$Au^{3+} + 3e^- \rightleftharpoons Au$	1.498

When a metal of more negative reduction potential (such as Mg) encounters an ion with a more positive reduction potential (such as Au), electron exchange takes place in a process called galvanic replacement (GR). GR has become a pillar of bi- and multimetallic NP synthesis in particular using Ag and Cu as sacrificial or semisacrificial templates.[104,105] Using Mg as a template is exciting because, in the metallic form, Mg has such a large negative standard reduction potential that it is expected to spontaneously exchange electrons with most metal ions except the alkali, alkali earth, and some lanthanides and actinides. Further, if not fully replaced, Mg can maintain plasmonic properties that can be combined with the other functionalities afforded by the added metal. This approach offers tremendous design opportunities covering the transition metals, post-transition metals, and metalloids, many of which have fascinating magnetic, catalytic, plasmonic, or electronic properties.

Mg NPs are so labile to replacement that Niu et al.[106,107] and Lui et al.[108] called them "superactive". They have shown that NPs produced by laser ablation of a Mg target can be used as a reducing agent for Au and Ag, with the obvious drawbacks of the setup complexities and lack of size/shape control associated with laser ablation. Colloidally synthesized Mg NPs bring a fresh breath of synthetic opportunities using the GR approach. In Asselin et al.,[109] we explore these exciting avenues and describe the synthesis of the bimetallics such as the plasmonic MgAu and MgAg and the plasmonic-catalysts MgPd and MgFe. The degree of replacement is stoichiometry-controlled, shown for Au, from potassium gold(III) chloride ($KAuCl_4$), in Figure 10. As more Au is added to the dry ethanolic solution, up to the full conversion stoichiometry of $2Au^{3+}$:$3Mg^0$ (0.67 Au equivalents), the characteristic ruby color of small Au NPs intensifies (Figure 10b) and increasing numbers of Au NPs can be seen on the Mg templates (bright in Figure 10g–k). Beyond 0.67 Au equivalents, full replacement occurs and leads to a collapse of the underlying structures (Figure 10l), as well as aggregation discernible by a loss of color (Figure 10b). In partially replaced NPs, the distribution of Mg metal is irregular and appears modulated, to some extent, by the position of the Au NPs (Figure 10c–f).

Partial GR of well-defined faceted Mg NPs can be extended to, in principle, most of the elements to the right of Mg in the periodic table. We performed GR of Mg by Ag, Fe, and Pd as a proof of this concept. Their immediate and straightforward success reinforces that Mg is a suitable platform for GR with most elements, providing a chemical form soluble in a nonaqueous solvent is chosen, here potassium tetrachloropalladate(II) (Na_2PdCl_4), silver nitrate ($AgNO_3$), and iron(III) chloride ($FeCl_3$) in ethanol. As for Au, these

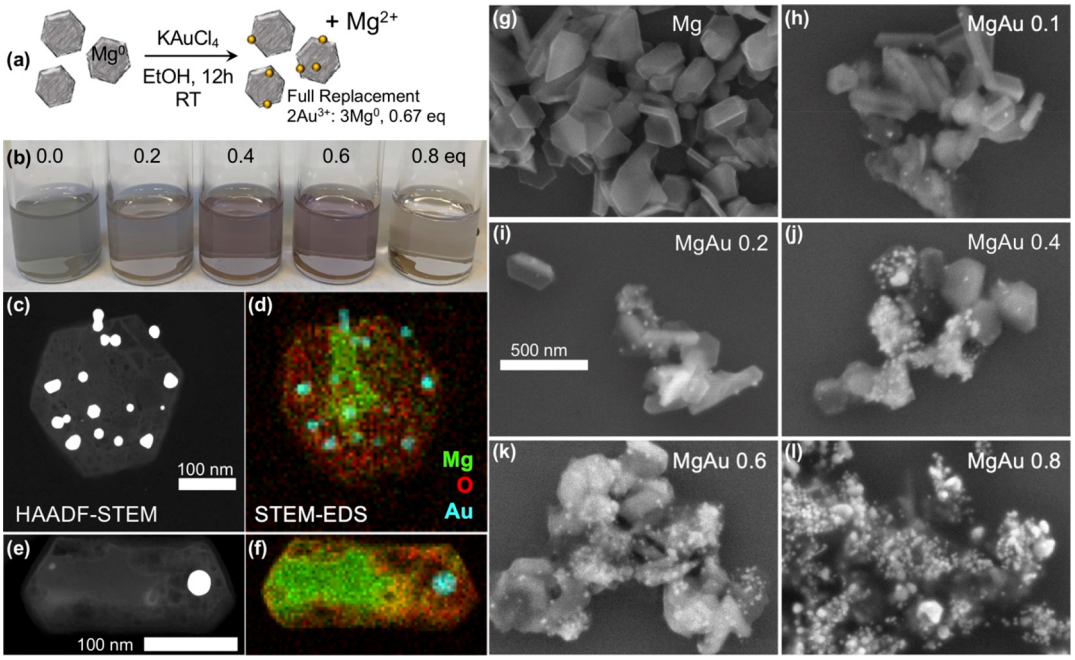

Figure 10. Galvanic replacement of colloidally synthesized Mg by Au in nonaqueous environment. (a) Reaction schematic. (b) Color change owing to the formation of Au NPs up to 0.6 equivalents (eq), and aggregation at 0.8 eq (c, e) HAADF-STEM images of decorated structures and (d, f) associated STEM-EDS elemental maps. (g–l) SEM images of GR products of Mg NPs by Au for different Au equivalents, all on the same scale as shown in (i). Adapted with permission from ref 109. Copyright 2019 AIP Publishing.

https://dx.doi.org/10.1021/acs.jpcc.0c03871
J. Phys. Chem. C 2020, 124, 15665−15679

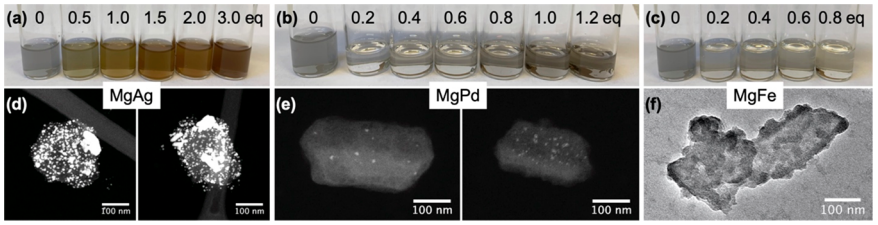

Figure 11. Partial galvanic replacement of Mg NPs leads to decorated bimetallic structures. The color change shown in the top panels indicates the gradual loss of Mg plasmonic response and the increase in the (a) Ag plasmonic signal and interband absorption in (b) Pd and (c) Fe. HAADF-STEM images of (d) MgAg and (e) MgPd and the TEM image of (f) MgFe show characteristic hexagonal or folded hexagonal templates. Decorations are of higher *Z* than Mg and thus appear brighter in HAADF-STEM (d, e) and darker in TEM (f). Adapted with permission from ref 109. Copyright 2019 AIP Publishing.

metals undergo GR and coalesce into small NPs that are found almost exclusively at the surface of the Mg template. Increasing the concentration of metal ions leads to an intensification of the optical signature of the decorating metal, plasmon resonances for Ag and interband absorption for Pd and Fe (Figure 11a–c). The density of decoration, and extent of Mg metal removal from the templates both increase with added metal ion. These effects were quantified to support the GR mechanism: ICP-MS showed increasing amounts of Mg in the supernatant with increasing metal addition, and UV–vis spectroscopy confirmed the disappearance of metal ions and the appearance of metallic NP signatures.[109]

The morphology of replaced structures from Mg appears significantly different from that obtained when Al NPs are used as sacrificial templates, as in Clay et al.[110] and Cui et al.[111] This is due, at least in part, to the different NP shapes, which tend to be sphere-like for FCC Al. Another key difference is that the GR reported here is nonaqueous, while that reported for Al is performed in concentrated aqueous NH_4Cl. This affects both the metal precursor speciation *via* pH control,[112] and the Al template's reactivity by inhibiting hydroxide formation. These initial results on the replacement of plasmonic Al and Mg NPs pave the way for an exciting array of synthetic approaches for bimetallic NPs.

Oxidation. Bulk Mg reacts with water and violently burns in air. Compounded with the enhanced surface area to volume ratio of NPs, this chemical reactivity appears to doom Mg's stability. To the contrary, the thin oxide formed at the surface of Mg NPs encapsulates the metallic core and bestows its stability in air and in most solvents except water. Figure 12 shows the spectroscopic characterization of this oxide layer on multiple NPs, all exposed to air during sample purification and preparation. STEM-EDS maps (Figure 12a–c) of hexagonal plates and a tent suggest a thickness of 20 nm; this is an upper bound given the delocalization of EDS as well as the sampling geometry through rounded edges. STEM-EELS maps are shown in Figure 12c alongside STEM-EDS maps for a hexagonal plate that suffered some etching. This allows the probing of three side facets and a rough estimation of the oxide layer thickness. The approximate full width at half-maximum for the oxygen peaks in the EDS line profile are, from left bottom to right top, 23, 14, and 20 nm; for EELS these are 24, 20, and 15 nm, again rough estimates given the 7 nm pixel distance. A more direct view of the oxide layer was obtained by milling a cross-section with a Ga ion beam, as shown in Figure 12d. The magnesium oxide thickness in this case is 6–7 nm, in line with the bulk values of a few to a few tens of nanometers.[113,114]

The effects of the oxide layer on plasmonic properties is difficult to probe experimentally, because thickness is heterogeneous even at the particle level, and growing a thicker oxide controllably has proven challenging. This can be explored numerically, however, as is shown in Figure 12e. MgO is an insulator with a dielectric constant of 1.7 in the visible;[115] adding increasingly thick layers to a 230 tip-to-tip, 30 nm thick hexagonal plate leads to a sequential red shift of the modes caused by the increase in local refractive index. The shape of the spectra, however, does not change, meaning that Mg metal retains its plasmonic properties even in the presence of the oxide. The scattering from a 230 wide, 30 nm thick NP coated on both sides with 20 nm of MgO retains more than half the intensity as that of an uncoated NP, albeit with a significant redshift. This aligns with computational results from Gutierrez et al., where a ∼100 nm red shift and no decrease in absorption cross-section is shown for a 40 nm radius sphere of Mg metal and a 20 nm metallic sphere coated with 20 nm of MgO. The oxide in Mg appears to be less detrimental than the oxide in Al: the same authors report a near-complete damping of the LSPR absorption for the 20 nm Al_2O_3 coated 20 nm radius Al sphere,[116] consistent with our own results on coated, truncated Al bipyramids.[70]

The core Mg is effectively encapsulated by this oxide layer such that it remains metallic and plasmonic. The oxide layer and underlying metal can be imaged directly in STEM, as shown in Figure 13a (dark field, DF) and at atomic resolution in Figure 13b (bright field, BF). The outer layer is cubic MgO viewed along its *c*-axis. The lattice spacing observed is 2.1 Å, corresponding to the {200} spacing in MgO; this oxide layer is less than 10 nm thick. The Mg is seen along the *c*-axis as well, displaying the expected hexagonal pattern and lattice spacing of ∼3 Å for the $\{10\bar{1}0\}$ planes. Further studies of the crystal structure and orientation using diffraction are reported in ref 62.

The metallic nature of the NP, critical for its plasmonic properties, has further been confirmed with EELS. Indeed, Mg, like Al, has a very strong bulk plasmon resonance in the low-loss region that can be used to quickly identify regions of metal vs oxide, as was done in Figures 7 and 12. The peak of this bulk plasmon resonance is located at 10.6 eV, as shown in Figure 13c. Further, the shape of the core-loss Mg peak indicates its oxidation state; a hydrogenic shape, i.e., with a sharp rise, characteristic of Mg metal is seen in the central parts of the NPs (Figure 13d), while a more structured spectrum was observed for the oxide-rich shell.[109]

The powder X-ray diffraction pattern of dried powder thinly spread on sticky tape shows the characteristic metallic Mg peaks at $2\theta \sim 32.2$, 34.4, 36.6, 47.8, 57.4, and 63.1°, corresponding to JCPDS 04-0770. The pattern obtained does not match either MgO (JCPDS 89-7746) nor $Mg(OH)_2$ (JCPDS 07-0239), suggesting the oxide layer present has very small domain size,

https://dx.doi.org/10.1021/acs.jpcc.0c03871
J. Phys. Chem. C 2020, 124, 15665–15679

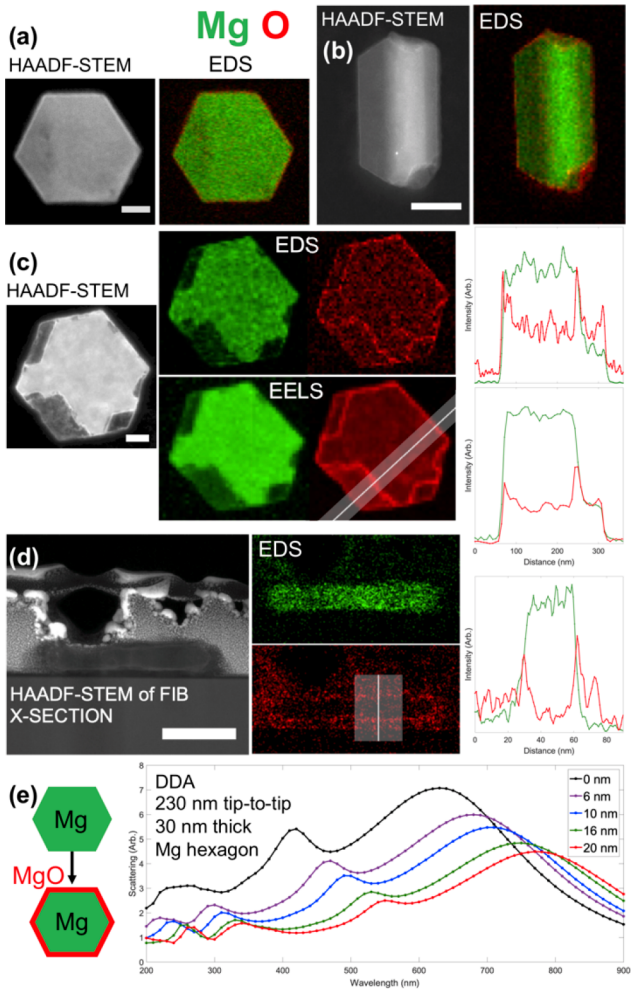

Figure 12. Spectroscopic characterization of the oxide layer formed on Mg NPs and its effect on the plasmonic behavior. HAADF-STEM and combined EDS maps of Mg and O Kα for (a) a hexagonal plate, (b) a tent NP. (c) HAADF-STEM and STEM-EDS maps of the Kα emission of Mg and O and STEM-EELS maps of the K absorption edge of Mg and O. The line profiles shown for EDS and EELS on the right were extracted and binned orthogonally along the same position shown as a white line in the O EELS map. (d) HAADF-STEM of a Pt-protected Mg hexagon cut as a thin cross-section by a Ga focused ion beam viewed perpendicular to the *c* axis, associated STEM-EDS maps of the Kα emission of Mg and O, and line profile extracted and binned orthogonally along the white line shown in the O EDS map. (e) DDA-calculated effect of the oxide layer on optical far-field scattering for a 30 nm thick, 230 nm tip-to-tip Mg metal hexagonal plate. Mg is colored green; O is colored red. Scale bars are 50 nm in (a) and (c) and 100 nm in (b) and (d). Adapted with permission from ref 109. Copyright 2019 AIP Publishing. Adapted with permission from refs 63 and 62. Copyrights 2018 and 2020 American Chemical Society.

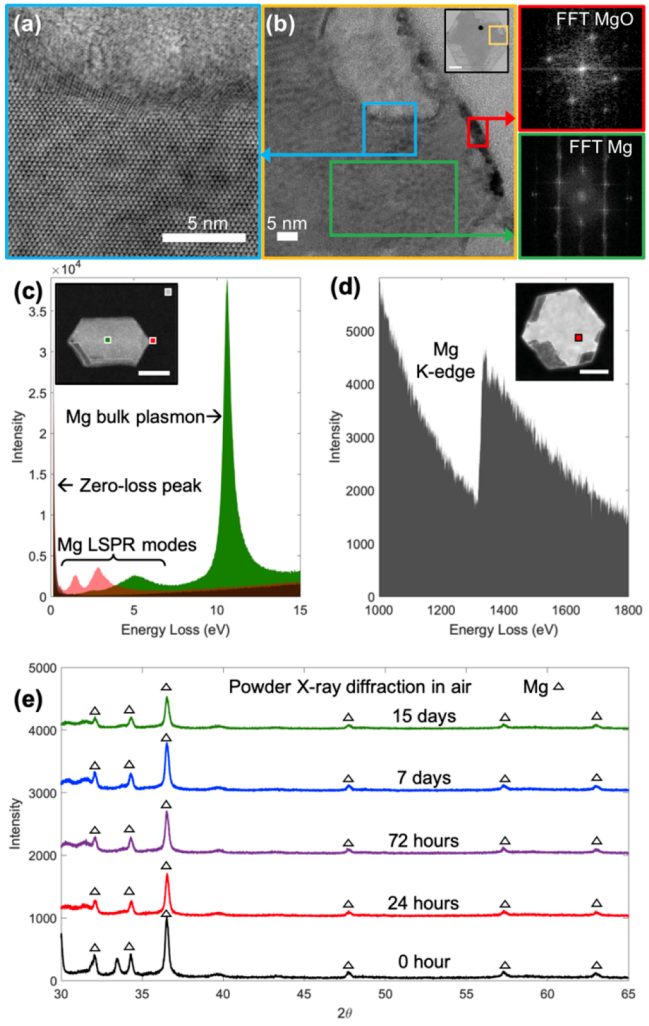

Figure 13. Presence and stability of Mg metal in Mg NPs. (a) DF-STEM of the region indicated in the inset from a NP galvanically replaced with Au. The scale bar in the inset is 50 nm. (b) Annular bright field (BF) image of the same region as in (a) and associated Fourier transforms showing Mg and MgO both viewed along the *c*-axis. EELS data show the presence, within the NP, of a (c) strong bulk plasmon and (d) hydrogenic K-edge shape, both characteristic of metallic Mg. The EEL spectrum positions are noted in the inset, where scale bars are 100 nm; the size of the square represents 4 times the acquisition area for clarity in (c) and the acquisition area in (d). (e) Powder X-ray diffraction pattern of Mg NPs in ambient air. Mg metal peaks are labeled with a triangle. Particles were stored in 2-propanol under Ar, deposited and dried in air, and then left in ambient air for the remainder of the experiment. Diffraction patterns were obtained immediately (red line) and at 24 h (purple line), 72 h (blue line), 7 days (green line), and 15 days (yellow line) after deposition. Panels c and e were adapted with permission from refs 62 and 63, respectively. Copyrights 2020 and 2018 American Chemical Society.

consistent with a polycrystalline, sub-10 nm shell. This oxide layer bequests Mg NPs their surprising stability, even in ambient air. The same sample periodically probed over 15 days while stored in ambient air does not show significant loss of Mg metal signal, as shown in Figure 13e. This stability in air is encouraging for the potential applications of Mg, although it is clear that its reactivity with water and hydroxide will pose significant challenges.

CONCLUSIONS AND OUTLOOK

Over the last 30 years the understanding of the shape, synthesis, and plasmonic applications of the noble metal Ag and Au has expanded to a mature field. The past decade has seen a growing interest in alternative materials for plasmonics and the emergence of, among others, Al. While some of the scientific knowledge acquired during this blooming of nanoplasmonics can be applied to the newcomer Mg, much remains to be studied and established, fueled by Mg's promise as an earth-abundant, full-spectrum alternative material.

https://dx.doi.org/10.1021/acs.jpcc.0c03871
J. Phys. Chem. C 2020, 124, 15665−15679

Here, recent advances on the understanding of shape, plasmonic properties, and chemical reactivity of Mg were discussed. Mg's HCP crystal structure is unusual for plasmonic metals (although common across the periodic table) and bestows on it a large array of potential twin planes, leading to peculiar shapes. Among those are folded and kite structures for monotwins, which are predicted by a modified Wulff construction and observed experimentally in colloidal mixtures. The far-field scattering and near-field light localization of these shapes was presented, highlighting that Mg firmly belongs to the plasmonic materials class and that its resonances can span the UV, visible, and near-IR. Lastly, detailed studies of the oxide layer and its protective effects as well as proof-of-concept results on the rich array of bimetallic NPs possible using partial galvanic replacement were described.

A significant challenge going forward is shape control. This is 2-fold, as twinning and growth are both key. Obtaining monodisperse samples first requires control over twinning in the early phases of nucleation and growth. The understanding of the thermodynamics of early nuclei formation is incomplete, with no "twinning phase diagram" such as those for Au yet available.[117,118] Experimental tools to control twinning in Mg also are yet to come; in noble metals, this is possible using an intermediate etching step in seed-mediated syntheses or surfactant control during nucleation.[119,120] Neither has been reported for Mg, and the latter is complicated by the strong reducing environment necessary for Mg reduction. Selective control of expressed facets, lending a given nuclei its final shape, is obtained for Au, Ag, and Al with the addition of surfactants or binding agents during growth; once again this is made difficult by the strong reducing environment in Mg's synthesis. Changing the Mg metal precursor and manipulating the availability of additional organometallic molecules and ligands, provided they are stable in the mixture, is a likely way forward. Once achieved, a rich range of anisotropic shape will be available, based on Mg's numerous twin planes and intrinsically anisotropic crystal lattice.

Adding to the richness of potential shapes, it is unlikely that we have explored all the possible twins of Mg; the $(11\bar{2}y)$-twinned structures with $y > 1$ remain experimentally elusive but promise additional kite-like NPs. Multiply twinned NPs are also in principle possible, yet only hinted at rather hesitantly, on the basis of a single experimental observation, by Ohno et al.[76] If realized, these would also provide pathways to new and unusual shapes, as they have done for Ag and Au.

There is also much to be learned about the use of Mg as a template for multifunctional materials, for instance through the creation of conformal thin shells, which could provide protection against degradation in water, as well as controlled decoration with additional metals. Control of the oxide formation during the multistep synthesis will be important, and etchants such as those used for Cu NPs[121] may play a role.

Mg and Mg-based bimetallic NPs have potential applications mapping on those of Al, Ag, and Au, while benefiting from full biocompatibility and a broad range response but suffering from high reactivity. As for Ag and Au 30 years ago, there remains vast unchartered territory on the understanding, control, and applications of Mg nanoplasmonics as sensors, photocatalysts, photothermal materials, field enhancers for spectroscopies, and many more.

AUTHOR INFORMATION

Corresponding Author

Emilie Ringe − *Department of Materials Science and Metallurgy, Department of Earth Sciences, University of Cambridge, Cambridge, United Kingdom CB2 3EQ;* orcid.org/0000-0003-3743-9204; Phone: +44 (0)1223 334330; Email: er407@cam.ac.uk; Fax: +44 (0)1223 334567

Complete contact information is available at: https://pubs.acs.org/10.1021/acs.jpcc.0c03871

Notes

The author declares no competing financial interest.

Biography

Photo provided by Tommy LaVergne

Emilie Ringe is a lecturer in multiscale, multidimensional imaging of synthetic and natural materials, jointly appointed in the Department of Earth Sciences and the Department of Materials Science and Metallurgy at the University of Cambridge. She obtained her Ph.D. from Northwestern University in 2012 and was a postdoctoral fellow at the University of Cambridge. In 2014, she joined Rice University's Department of Materials Science and NanoEngineering and Department of Chemistry as an assistant professor, where she established the Electron Microscopy Center. She moved back to Cambridge in 2018, where she pursues her research on earth-abundant plasmonic materials, optical nanostructures, electron microscopy, and heterogeneous light-driven catalysis.

ACKNOWLEDGMENTS

This work was supported by the EU Framework Programme for Research and Innovation Horizon 2020 (Starting Grant SPECs 804523), 3M (Non-Tenured Faculty Award), Engineering and Physical Sciences Research Council (EP/R513180/1 and EP/L015978/1), Natural Sciences and Engineering Research Council of Canada and Fonds de Recherche Québec − Nature et Technologies (BP and B3X programs). Thanks to Christina Boukouvala, Elizabeth R. Hopper, Jérémie Asselin, Quentin Ramasse, John S. Biggins, and Aimé-Jean Lavigne for helpful discussions and support.

REFERENCES

(1) Martin, R. C.; Locatelli, E.; Li, Y.; Matteini, P.; Monaco, I.; Cui, G.; Li, S.; Banchelli, M.; Pini, R.; Comes Franchini, M. One-Pot Synthesis of Magnesium Nanoparticles Embedded in a Chitosan Microparticle Matrix: a Highly Biocompatible Tool for in Vivo Cancer Treatment. *J. Mater. Chem. B* **2016**, *4*, 207−211.

(2) Jiang, T.; Song, J.; Zhang, W.; Wang, H.; Li, X.; Xia, R.; Zhu, L.; Xu, X. Au−Ag@Au Hollow Nanostructure with Enhanced Chemical

Stability and Improved Photothermal Transduction Efficiency for Cancer Treatment. *ACS Appl. Mater. Interfaces* **2015**, *7*, 21985−21994.
(3) Jang, H.; Kim, Y.-K.; Huh, H.; Min, D.-H. Facile Synthesis and Intraparticle Self-Catalytic Oxidation of Dextran-Coated Hollow Au−Ag Nanoshell and Its Application for Chemo-Thermotherapy. *ACS Nano* **2014**, *8*, 467−475.
(4) Gobin, A. M.; Lee, M. H.; Halas, N. J.; James, W. D.; Drezek, R. A.; West, J. L. Near-Infrared Resonant Nanoshells for Combined Optical Imaging and Photothermal Cancer Therapy. *Nano Lett.* **2007**, *7*, 1929−1934.
(5) Locatelli, E.; Matteini, P.; Sasdelli, F.; Pucci, A.; Chiariello, M.; Molinari, V.; Pini, R.; Comes Franchini, M. Surface Chemistry and Entrapment of Magnesium Nanoparticles into Polymeric Micelles: a Highly Biocompatible Tool for Photothermal Therapy. *Chem. Commun.* **2014**, *50*, 7783−7786.
(6) Sharma, B.; Frontiera, R. R.; Henry, A.-I.; Ringe, E.; Van Duyne, R. P. SERS: Materials, Applications, and the Future. *Mater. Today* **2012**, *15*, 16−25.
(7) Rainville, L.; Dorais, M.-C.; Boudreau, D. Controlled Synthesis of Low Polydispersity Ag@SiO_2 Core-Shell Nanoparticles for use in Plasmonic Applications. *RSC Adv.* **2013**, *3*, 13953−13960.
(8) Lakowicz, J. R. Radiative Decay Engineering 5: Metal-Enhanced Fluorescence and Plasmon Emission. *Anal. Biochem.* **2005**, *337*, 171−194.
(9) Lakowicz, J. R.; Geddes, C. D.; Gryczynski, I.; Malicka, J.; Gryczynski, Z.; Alsan, K.; Lukomska, J.; Matveeva, E.; Zhang, J.; Badugu, R.; et al. Advances in Surface-Enhanced Fluorescence. *J. Fluoresc.* **2004**, *14*, 425−441.
(10) Stiles, P. L.; Dieringer, J. A.; Shah, N. C.; Van Duyne, R. P. Surface-Enhanced Raman Spectroscopy. *Annu. Rev. Anal. Chem.* **2008**, *1*, 601−626.
(11) Asselin, J.; Viger, M. L.; Boudreau, D. Metal-Enhanced Fluorescence and FRET in Multilayer Core-Shell Nanoparticles. *Adv. Chem.* **2014**, *2014*, 812313.
(12) Zhang, Y.; Yang, P.; Habeeb Muhammed, M. A.; Alsaiari, S. K.; Moosa, B.; Almalik, A.; Kumar, A.; Ringe, E.; Khashab, N. M. Tunable and Linker Free Nanogaps in Core−Shell Plasmonic Nanorods for Selective and Quantitative Detection of Circulating Tumor Cells by SERS. *ACS Appl. Mater. Interfaces* **2017**, *9*, 37597−37605.
(13) Szunerits, S.; Boukherroub, R. Sensing using Localised Surface Plasmon Resonance Sensors. *Chem. Commun.* **2012**, *48*, 8999−9010.
(14) Mayer, K. M.; Hafner, J. H. Localized Surface Plasmon Resonance Sensors. *Chem. Rev.* **2011**, *111*, 3828−3857.
(15) Sepulveda, B.; Angelome, P. C.; Lechuga, L. M.; Liz-Marzán, L. M. LSPR-Based Nanobiosensors. *Nano Today* **2009**, *4*, 244−251.
(16) Anker, J. N.; Hall, W. P.; Lyandres, O.; Shah, N. C.; Zhao, J.; Van Duyne, R. P. Biosensing with Plasmonic Nanosensors. *Nat. Mater.* **2008**, *7*, 442−453.
(17) Lu, M.; Zhu, H.; Bazuin, C. G.; Peng, W.; Masson, J.-F. Polymer-Templated Gold Nanoparticles on Optical Fibers for Enhanced-Sensitivity Localized Surface Plasmon Resonance Biosensors. *ACS sensors* **2019**, *4*, 613−622.
(18) Guo, X.; Hao, C.; Jin, G.; Zhu, H. Y.; Guo, X. Y. Copper Nanoparticles on Graphene Support: an Efficient Photocatalyst for Coupling of Nitroaromatics in Visible Light. *Angew. Chem., Int. Ed.* **2014**, *53*, 1973−1977.
(19) Swearer, D. F.; Zhao, H.; Zhou, L.; Zhang, C.; Robatjazi, H.; Martirez, J. M. P.; Krauter, C. M.; Yazdi, S.; McClain, M. J.; Ringe, E.; et al. Heterometallic Antenna−Reactor Complexes for Photocatalysis. *Proc. Natl. Acad. Sci. U. S. A.* **2016**, *113*, 8916−8920.
(20) Christopher, P.; Xin, H.; Linic, S. Visible-Light-Enhanced Catalytic Oxidation Reactions on Plasmonic Silver Nanostructures. *Nat. Chem.* **2011**, *3*, 467.
(21) Brongersma, M. L.; Halas, N. J.; Nordlander, P. Plasmon-Induced Hot Carrier Science and Technology. *Nat. Nanotechnol.* **2015**, *10*, 25.
(22) Zheng, Z.; Tachikawa, T.; Majima, T. Single-particle study of Pt-modified Au nanorods for plasmon-enhanced hydrogen generation in visible to near-infrared region. *J. Am. Chem. Soc.* **2014**, *136*, 6870−6873.
(23) Marimuthu, A.; Zhang, J.; Linic, S. Tuning Selectivity in Propylene Epoxidation by Plasmon Mediated Photo-Switching of Cu Oxidation State. *Science* **2013**, *339*, 1590−1593.
(24) Maier, S. A.; Kik, P. G.; Atwater, H. A.; Meltzer, S.; Harel, E.; Koel, B. E.; Requicha, A. A. Local Detection of Electromagnetic Energy Transport below the Diffraction Limit in Metal Nanoparticle Plasmon Waveguides. *Nat. Mater.* **2003**, *2*, 229−232.
(25) Maier, S. A.; Brongersma, M. L.; Kik, P. G.; Meltzer, S.; Requicha, A. A.; Atwater, H. A. Plasmonics—A Route to Nanoscale Optical Devices. *Adv. Mater.* **2001**, *13*, 1501−1505.
(26) Tcherniak, A.; Ha, J.; Dominguez-Medina, S.; Slaughter, L.; Link, S. Probing a Century Old Prediction one Plasmonic Particle at a Time. *Nano Lett.* **2010**, *10*, 1398−1404.
(27) Tuersun, P.; Han, X. e. Optical Absorption Analysis and Optimization of Gold Nanoshells. *Appl. Opt.* **2013**, *52*, 1325−1329.
(28) Cobley, C. M.; Au, L.; Chen, J.; Xia, Y. Targeting Gold Nanocages to Cancer Cells for Photothermal Destruction and Drug Delivery. *Expert Opin. Drug Delivery* **2010**, *7*, 577−587.
(29) Whitney, A. V.; Elam, J. W.; Zou, S.; Zinovev, A. V.; Stair, P. C.; Schatz, G. C.; Van Duyne, R. P. Localized Surface Plasmon Resonance Nanosensor: a High-Resolution Distance-Dependence Study using Atomic Layer Deposition. *J. Phys. Chem. B* **2005**, *109*, 20522−20528.
(30) Kaminska, I.; Maurer, T.; Nicolas, R.; Renault, M.; Lerond, T.; Salas-Montiel, R.; Herro, Z.; Kazan, M.; Niedziolka-Jönsson, J.; Plain, J. Near-Field and Far-Field Sensitivities of LSPR Sensors. *J. Phys. Chem. C* **2015**, *119*, 9470−9476.
(31) Cai, W.; Zhong, H.; Zhang, L. Optical Measurements of Oxidation Behavior of Silver Nanometer Particle within Pores of Silica Host. *J. Appl. Phys.* **1998**, *83*, 1705−1710.
(32) McMahon, M.; Lopez, R.; Meyer, H.; Feldman, L. C.; Haglund, R. Rapid Tarnishing of Silver Nanoparticles in Ambient Laboratory Air. *Appl. Phys. B: Lasers Opt.* **2005**, *80*, 915−921.
(33) Blaber, M. G.; Arnold, M. D.; Ford, M. J. A Review of the Optical Properties of Alloys and Intermetallics for Plasmonics. *J. Phys.: Condens. Matter* **2010**, *22*, 143201.
(34) Palik, E. D. *Handbook of Optical Constants of Solids III*; Academic Press: New York, 1998.
(35) Johnson, P. B.; Christy, R. W. Optical Constants of the Noble Metal. *Phys. Rev. B* **1972**, *6*, 4370.
(36) Rakić, A. D. Algorithm for the Determination of Intrinsic Optical Constants of Metal Films: Application to Aluminum. *Appl. Opt.* **1995**, *34*, 4755−4767.
(37) Gutiérrez, Y.; Losurdo, M.; González, F.; Everitt, H. O.; Moreno, F. Nanoplasmonic Photothermal Heating and Near-Field Enhancements: A Comparative Survey of 19 Metals. *J. Phys. Chem. C* **2020**, *124*, 7386−7395.
(38) Gonzalez-Posada, F.; Sellappan, R.; Vanpoucke, B.; Chakarov, D. Oxidation of Copper Nanoparticles in Water Monitored in Situ by Localized Surface Plasmon Resonance Spectroscopy. *RSC Adv.* **2014**, *4*, 20659−20664.
(39) Rice, K. P.; Walker, E. J., Jr; Stoykovich, M. P.; Saunders, A. E. Solvent-Dependent Surface Plasmon Response and Oxidation of Copper Nanocrystals. *J. Phys. Chem. C* **2011**, *115*, 1793−1799.
(40) Chan, G. H.; Zhao, J.; Schatz, G. C.; Van Duyne, R. P. Localized Surface Plasmon Resonance Spectroscopy of Triangular Aluminum Nanoparticles. *J. Phys. Chem. C* **2008**, *112*, 13958−13963.
(41) Knight, M. W.; King, N. S.; Liu, L.; Everitt, H. O.; Nordlander, P.; Halas, N. J. Aluminum for Plasmonics. *ACS Nano* **2014**, *8*, 834−840.
(42) McClain, M. J.; Schlather, A. E.; Ringe, E.; King, N. S.; Liu, L.; Manjavacas, A.; Knight, M. W.; Kumar, I.; Whitmire, K. H.; Everitt, H. O. Aluminum Nanocrystals. *Nano Lett.* **2015**, *15*, 2751−2755.
(43) Creighton, J. A.; Eadon, D. G. Ultraviolet−Visible Absorption Spectra of the Colloidal Metallic Elements. *J. Chem. Soc., Faraday Trans.* **1991**, *87*, 3881−3891.
(44) Kim, S.; Kim, J. M.; Park, J. E.; Nam, J. M. Nonnoble-Metal-Based Plasmonic Nanomaterials: Recent Advances and Future Perspectives. *Adv. Mater.* **2018**, *30*, 1704528.
(45) Sanz, J. M.; Ortiz, D.; Alcaraz de la Osa, R.; Saiz, J. M.; González, F.; Brown, A. S.; Losurdo, M.; Everitt, H. O.; Moreno, F. UV Plasmonic

Behavior of Various Metal Nanoparticles in the Near- and Far-Field Regimes: Geometry and Substrate Effects. *J. Phys. Chem. C* **2013**, *117*, 19606−19615.
(46) Yang, Y.; Callahan, J. M.; Kim, T.-H.; Brown, A. S.; Everitt, H. O. Ultraviolet Nanoplasmonics: a Demonstration of Surface-Enhanced Raman Spectroscopy, Fluorescence, and Photodegradation using Gallium Nanoparticles. *Nano Lett.* **2013**, *13*, 2837−2841.
(47) Watson, A. M.; Zhang, X.; Alcaraz de La Osa, R.; Sanz, J. M.; Gonza′lez, F.; Moreno, F.; Finkelstein, G.; Liu, J.; Everitt, H. O. Rhodium Nanoparticles for Ultraviolet Plasmonics. *Nano Lett.* **2015**, *15*, 1095−1100.
(48) Kanehara, M.; Koike, H.; Yoshinaga, T.; Teranishi, T. Indium Tin Oxide Nanoparticles with Compositionally Tunable Surface Plasmon Resonance Frequencies in the Near-IR Region. *J. Am. Chem. Soc.* **2009**, *131*, 17736−17737.
(49) Jeong, H.-H.; Mark, A. G.; Fischer, P. Magnesium Plasmonics for UV Applications and Chiral Sensing. *Chem. Commun.* **2016**, *52*, 12179−12182.
(50) Sterl, F.; Strohfeldt, N.; Walter, R.; Griessen, R.; Tittl, A.; Giessen, H. Magnesium as Novel Material for Active Plasmonics in the Visible Wavelength Range. *Nano Lett.* **2015**, *15*, 7949−7955.
(51) Wang, Y.; Peterson, E. M.; Harris, J. M.; Appusamy, K.; Guruswamy, S.; Blair, S. Magnesium as a Novel UV Plasmonic Material for Fluorescence Decay Rate Engineering in Free Solution. *J. Phys. Chem. C* **2017**, *121*, 11650−11657.
(52) Sterl, F.; Linnenbank, H.; Steinle, T.; Mörz, F.; Strohfeldt, N.; Giessen, H. Nanoscale Hydrogenography on Single Magnesium Nanoparticles. *Nano Lett.* **2018**, *18*, 4293−4302.
(53) Duan, X.; Kamin, S.; Sterl, F.; Giessen, H.; Liu, N. Hydrogen-Regulated Chiral Nanoplasmonics. *Nano Lett.* **2016**, *16*, 1462−1466.
(54) Liu, W.; Aguey-Zinsou, K.-F. Size Effects and Hydrogen Storage Properties of Mg Nanoparticles Synthesised by an Electroless Reduction Method. *J. Mater. Chem. A* **2014**, *2*, 9718−9726.
(55) Zaluska, A.; Zaluski, L.; Ström−Olsen, J. Nanocrystalline Magnesium for Hydrogen Storage. *J. Alloys Compd.* **1999**, *288*, 217−225.
(56) Jeon, K.-J.; Moon, H. R.; Ruminski, A. M.; Jiang, B.; Kisielowski, C.; Bardhan, R.; Urban, J. J. Air-Stable Magnesium Nanocomposites Provide Rapid and High-Capacity Hydrogen Storage without using Heavy-Metal Catalysts. *Nat. Mater.* **2011**, *10*, 286.
(57) Duan, X.; Liu, N. Magnesium for Dynamic Nanoplasmonics. *Acc. Chem. Res.* **2019**, *52*, 1979−1989.
(58) Duan, X.; Kamin, S.; Liu, N. Dynamic Plasmonic Colour Display. *Nat. Commun.* **2017**, *8*, 14606.
(59) Farinha, T. G.; Gong, C.; Benson, Z. A.; Leite, M. S. Magnesium for Transient Photonics. *ACS Photonics* **2019**, *6*, 272−278.
(60) Yi, C.; Su, M.-N.; Dongare, P. D.; Chakraborty, D.; Cai, Y.-Y.; Marolf, D. M.; Kress, R. N.; Ostovar, B.; Tauzin, L. J.; Wen, F.; et al. Polycrystallinity of Lithographically Fabricated Plasmonic Nanostructures Dominates Their Acoustic Vibrational Damping. *Nano Lett.* **2018**, *18*, 3494−3501.
(61) Rodríguez-Fernández, J.; Funston, A. M.; Pérez-Juste, J.; Álvarez-Puebla, R. A.; Liz-Marzán, L. M.; Mulvaney, P. The Effect of Surface Roughness on the Plasmonic Response of Individual Sub-Micron Gold Spheres. *Phys. Chem. Chem. Phys.* **2009**, *11*, 5909−5914.
(62) Asselin, J.; Boukouvala, C.; Hopper, E. R.; Ramasse, Q. M.; Biggins, J. S.; Ringe, E. Tents, Chairs, Tacos, Kites, and Rods: Shapes and Plasmonic Properties of Singly Twinned Magnesium Nanoparticles. *ACS Nano* **2020**, *14*, 5968.
(63) Biggins, J. S.; Yazdi, S.; Ringe, E. Magnesium Nanoparticle Plasmonics. *Nano Lett.* **2018**, *18*, 3752−3758.
(64) Morss, L. R.; Edelstein, N. M.; Fuger, J.; Katz, J. J. *The Chemistry of the Actinide and Transactinide Elements*; Springer: Dordrecht, 2006.
(65) Greenwood, N. N.; Earnshaw, A. *Chemistry of the Elements*, 2nd ed.; Elsevier Butterworth-Heinemann: Oxford, 1997.
(66) Hammond, C. *The Basics of Crystallography and Diffraction*; International Union of Crystallography, OUP: Oxford, 2009.
(67) Wulff, G. XXVI. Zur Theorie des Krystallhabitus. *Z. Kristallogr. - Cryst. Mater.* **1908**, *45*, 433−472.
(68) Marks, L. Modified Wulff Constructions for Twinned Particles. *J. Cryst. Growth* **1983**, *61*, 556−566.
(69) Ringe, E.; Van Duyne, R. P.; Marks, L. D. Kinetic and Thermodynamic Modified Wulff Constructions for Twinned Nanoparticles. *J. Phys. Chem. C* **2013**, *117*, 15859−15870.
(70) Boukouvala, C.; Ringe, E. Wulff-Based Approach to Modeling the Plasmonic Response of Single Crystal, Twinned, and Core−Shell Nanoparticles. *J. Phys. Chem. C* **2019**, *123*, 25501−25508.
(71) Flatau, P.; Draine, B. T. Fast Near Field Calculations in the Discrete Dipole Approximation for Regular Rectilinear Grids. *Opt. Express* **2012**, *20*, 1247−1252.
(72) Draine, B. T.; Flatau, P. J. Discrete-Dipole Approximation for Periodic Targets: Theory and Tests. *J. Opt. Soc. Am. A* **2008**, *25*, 2693−2703.
(73) Draine, B. T.; Flatau, P. J. Discrete-Dipole Approximation for Scattering Calculations. *J. Opt. Soc. Am. A* **1994**, *11*, 1491−1499.
(74) Bigelow, N. W.; Vaschillo, A.; Iberi, V.; Camden, J. P.; Masiello, D. J. Characterization of the Electron-and Photon-Driven Plasmonic Excitations of Metal Nanorods. *ACS Nano* **2012**, *6*, 7497−7504.
(75) Partridge, P. The Crystallography and Deformation Modes of Hexagonal Close-Packed Metals. *Metall. Rev.* **1967**, *12*, 169−194.
(76) Ohno, T.; Yamauchi, K. Magnesium Twinned Particles Grown in Inert Gases. *Jpn. J. Appl. Phys.* **1981**, *20*, 1385.
(77) Schatz, G. C.; Van Duyne, R. P. Electromagnetic Mechanism of Surface-Enhanced Spectroscopy. In *Handbook of Vibrational Spectroscopy*; Chalmers, J. M., Griffiths, P. R., Eds.; Wiley: Chichester, 2002; Vol. *1*, pp 759−774.
(78) Jackson, J. D. *Classical Electrodynamics*, 3rd ed.; John Wiley & Sons Inc.: New York, NY, 1999.
(79) Gérard, D.; Gray, S. K. Aluminium Plasmonics. *J. Phys. D: Appl. Phys.* **2015**, *48*, 184001.
(80) *Standard Tables for Reference Solar Spectral Irradiances: Direct Normal and Hemispherical on 37° Tilted Surface*; ASTM International: West Conshohocken, PA, 2012; Vol. ASTM G173-03(2012).
(81) Hu, M.; Novo, C.; Funston, A.; Wang, H.; Staleva, H.; Zou, S.; Mulvaney, P.; Xia, Y.; Hartland, G. V. Dark-Field Microscopy Studies of Single Metal Nanoparticles: Understanding the Factors that Influence the Linewidth of the Localized Surface Plasmon Resonance. *J. Mater. Chem.* **2008**, *18*, 1949−1960.
(82) Flaten, C. J.; Stern, E. A. Optical Constants of Some Silver Alloys. *Phys. Rev. B* **1975**, *11*, 638−650.
(83) Sau, T. K.; Murphy, C. J. Room Temperature, High-Yield Synthesis of Multiple Shapes of Gold Nanoparticles in Aqueous Solution. *J. Am. Chem. Soc.* **2004**, *126*, 8648−8649.
(84) Jana, N. R. Gram-Scale Synthesis of Soluble, Near-Monodisperse Gold Nanorods and Other Anisotropic Nanoparticles. *Small* **2005**, *1*, 875−882.
(85) Ye, X.; Jin, L.; Caglayan, H.; Chen, J.; Xing, G.; Zheng, C.; Doan-Nguyen, V.; Kang, Y.; Engheta, N.; Kagan, C. R.; et al. Improved Size-Tunable Synthesis of Monodisperse Gold Nanorods through the Use of Aromatic Additives. *ACS Nano* **2012**, *6*, 2804−2817.
(86) Wang, H.; Fu, K.; Drezek, R. A.; Halas, N. J. Light Scattering from Spherical Plasmonic Nanoantennas: Effects of Nanoscale Roughness. *Appl. Phys. B: Lasers Opt.* **2006**, *84*, 191−195.
(87) Zhang, F.; Martin, J.; Plain, J. Long-Term Stability of Plasmonic Resonances Sustained by Evaporated Aluminum Nanostructures. *Opt. Mater. Express* **2019**, *9*, 85−94.
(88) Kumar, A.; Villarreal, E.; Zhang, X.; Ringe, E. Micro-Extinction Spectroscopy (MExS): a Versatile Optical Characterization Technique. *Adv. Struct. Chem. Imaging* **2018**, *4*, 8.
(89) Ringe, E.; Sharma, B.; Henry, A.-I.; Marks, L. D.; Van Duyne, R. P. Single nanoparticle plasmonics. *Phys. Chem. Chem. Phys.* **2013**, *15*, 4110−4129.
(90) Henry, A.-I.; Bingham, J. M.; Ringe, E.; Marks, L. D.; Schatz, G. C.; Van Duyne, R. P. Correlated Structure and Optical Property Studies of Plasmonic Nanoparticles. *J. Phys. Chem. C* **2011**, *115*, 9291−9305.
(91) Mock, J. J.; Barbic, M.; Smith, D. R.; Schultz, D. A.; Schultz, S. Shape Effects in Plasmon Resonance of Individual Colloidal Silver Nanoparticles. *J. Chem. Phys.* **2002**, *116*, 6755−6759.

https://dx.doi.org/10.1021/acs.jpcc.0c03871
J. Phys. Chem. C 2020, 124, 15665−15679

(92) Kociak, M.; Stéphan, O. Mapping Plasmons at the Nanometer Scale in an Electron Microscope. *Chem. Soc. Rev.* **2014**, *43*, 3865−3883.
(93) Cherqui, C.; Thakkar, N.; Li, G.; Camden, J. P.; Masiello, D. J. Characterizing Localized Surface Plasmons Using Electron Energy-Loss Spectroscopy. *Annu. Rev. Phys. Chem.* **2016**, *67*, 331−357.
(94) Garcia de Abajo, F. J. Optical Excitations in Electron Microscopy. *Rev. Mod. Phys.* **2010**, *82*, 209.
(95) Song, M.-R.; Chen, M.; Zhang, Z.-J. Preparation and Characterization of Mg Nanoparticles. *Mater. Charact.* **2008**, *59*, 514−518.
(96) Viyannalage, L.; Lee, V.; Dennis, R. V.; Kapoor, D.; Haines, C. D.; Banerjee, S. From Grignard's Reagents to Well-Defined Mg Nanostructures: Distinctive Electrochemical and Solution Reduction Routes. *Chem. Commun.* **2012**, *48*, 5169−5171.
(97) Bauer, L.; Reiss, E. L. Cutoff Wavenumbers and Modes of Hexagonal Waveguides. *SIAM J. Appl. Math.* **1978**, *35*, 508−514.
(98) Schmidt, F.-P.; Ditlbacher, H.; Hohenester, U.; Hohenau, A.; Hofer, F.; Krenn, J. R. Dark Plasmonic Breathing Modes in Silver Nanodisks. *Nano Lett.* **2012**, *12*, 5780−5783.
(99) Ringe, E.; DeSantis, C. J.; Collins, S. M.; Duchamp, M.; Dunin-Borkowski, R. E.; Skrabalak, S. E.; Midgley, P. A. Resonances of Nanoparticles with Poor Plasmonic Metal Tips. *Sci. Rep.* **2015**, *5*, 17431.
(100) Leary, R. K.; Kumar, A.; Straney, P. J.; Collins, S. M.; Yazdi, S.; Dunin-Borkowski, R. E.; Midgley, P. A.; Millstone, J. E.; Ringe, E. Structural and Optical Properties of Discrete Dendritic Pt Nanoparticles on Colloidal Au Nanoprisms. *J. Phys. Chem. C* **2016**, *120*, 20843−20851.
(101) Collins, S. M.; Ringe, E.; Duchamp, M.; Saghi, Z.; Dunin-Borkowski, R. E.; Midgley, P. A. Eigenmode Tomography of Surface Charge Oscillations of Plasmonic Nanoparticles by Electron Energy Loss Spectroscopy. *ACS Photonics* **2015**, *2*, 1628−1635.
(102) Ringe, E.; Langille, M. R.; Sohn, K.; Zhang, J.; Huang, J.; Mirkin, C. A.; Van Duyne, R. P.; Marks, L. D. Plasmon Length: A Universal Parameter to Describe Size Effects in Gold Nanoparticles. *J. Phys. Chem. Lett.* **2012**, *3*, 1479−1483.
(103) *CRC Handbook of Chemistry and Physics*, 92nd ed.; Haynes, W. M., Ed.; CRC Press: Boca Raton, FL, 2011; pp 5-80−5-89.
(104) Xia, X.; Wang, Y.; Ruditskiy, A.; Xia, Y. 25th Anniversary Article: Galvanic Replacement: A Simple and Versatile Route to Hollow Nanostructures with Tunable and Well-Controlled Properties. *Adv. Mater.* **2013**, *25*, 6313−6333.
(105) Lu, X.; Chen, J.; Skrabalak, S. E.; Xia, Y. Galvanic Replacement Reaction: A Simple and Powerful Route to Hollow and Porous Metal Nanostructures. *Proc. Inst. Mech. Eng., Part N* **2007**, *221*, 1.
(106) Niu, K.; Yang, J.; Kulinich, S.; Sun, J.; Du, X. Hollow Nanoparticles of Metal Oxides and Sulfides: Fast Preparation via Laser Ablation in Liquid. *Langmuir* **2010**, *26*, 16652−16657.
(107) Niu, K. Y.; Kulinich, S. A.; Yang, J.; Zhu, A. L.; Du, X. W. Galvanic Replacement Reactions of Active-Metal Nanoparticles. *Chem. - Eur. J.* **2012**, *18*, 4234−4241.
(108) Li, X.; Liu, H.; Yang, J.; Qiao, S.-Z.; Du, X.-W. Pure Gold Nanocages by Galvanic Replacement Reaction of Magnesium Nanoparticles. *RSC Adv.* **2014**, *4*, 1185−1188.
(109) Asselin, J.; Boukouvala, C.; Wu, Y.; Hopper, E. R.; Collins, S. M.; Biggins, J. S.; Ringe, E. Decoration of Plasmonic Mg Nanoparticles by Partial Galvanic Replacement. *J. Chem. Phys.* **2019**, *151*, 244708.
(110) Clay, M.; Cui, Q.; Sha, Y.; Chen, J.; Rondinone, A. J.; Wu, Z.; Chen, J.; Gu, Z. Galvanic Synthesis of Bi-Modal Porous Metal Nanostructures Using Aluminum Nanoparticle Templates. *Mater. Lett.* **2012**, *88*, 143−147.
(111) Cui, Q.; Sha, Y.; Chen, J.; Gu, Z. Galvanic Synthesis of Hollow Non-Precious Metal Nanoparticles using Aluminum Nanoparticle Template and Their Catalytic Applications. *J. Nanopart. Res.* **2011**, *13*, 4785−4794.
(112) Daniel, J. R.; McCarthy, L. A.; Ringe, E.; Boudreau, D. Enhanced Control of Plasmonic Properties of Silver−Gold Hollow Nanoparticles via a Reduction-Assisted Galvanic Replacement Approach. *RSC Adv.* **2019**, *9*, 389−396.
(113) Feliu, S., Jr; Galván, J.; Pardo, A.; Merino, M.; Arrabal, R. Native Air-Formed Oxide Film and its Effect on Magnesium Alloys Corrosion. *Open Corros. J.* **2010**, *3*, 80−90.
(114) Nordlien, J. H.; Ono, S.; Masuko, N.; Nisancioglu, K. A TEM Investigation of Naturally Formed Oxide Films on Pure Magnesium. *Corros. Sci.* **1997**, *39*, 1397−1414.
(115) Stephens, R. E.; Malitson, I. H. Index of Refraction of Magnesium Oxide. *J. Res. Natl. Bur. Stand.* **1952**, *49*, 249−252.
(116) Gutierrez, Y.; Ortiz, D.; Sanz, J. M.; Saiz, J. M.; Gonzalez, F.; Everitt, H. O.; Moreno, F. How an Oxide Shell Affects the Ultraviolet Plasmonic Behavior of Ga, Mg, and Al Nanostructures. *Opt. Express* **2016**, *24*, 20621−20631.
(117) Baletto, F.; Ferrando, R.; Fortunelli, A.; Montalenti, F.; Mottet, C. Crossover among Structural Motifs in Transition and Noble-Metal Clusters. *J. Chem. Phys.* **2002**, *116*, 3856−3863.
(118) Baletto, F.; Ferrando, R. Structural Properties of Nanoclusters: Energetic, Thermodynamic, and Kinetic Effects. *Rev. Mod. Phys.* **2005**, *77*, 371−423.
(119) Xia, Y.; Xiong, Y.; Lim, B.; Skrabalak, S. E. Shape-Controlled Synthesis of Metal Nanocrystals: Simple Chemistry Meets Complex Physics? *Angew. Chem., Int. Ed.* **2009**, *48*, 60−103.
(120) Wiley, B.; Herricks, T.; Sun, Y.; Xia, Y. Polyol Synthesis of Silver Nanoparticles: Use of Chloride and Oxygen to Promote the Formation of Single-Crystal, Truncated Cubes and Tetrahedrons. *Nano Lett.* **2004**, *4*, 1733−1739.
(121) Chan, G. H.; Zhao, J.; Hicks, E. M.; Schatz, G. C.; Van Duyne, R. P. Plasmonic Properties of Copper Nanoparticles Fabricated by Nanosphere Lithography. *Nano Lett.* **2007**, *7*, 1947−1952.

https://dx.doi.org/10.1021/acs.jpcc.0c03871
J. Phys. Chem. C 2020, 124, 15665−15679